Icarus 210 (2010) 545–565

Contents lists available at ScienceDirect

Icarus

journal homepage: www.elsevier.com/locate/icarus

THEMIS-VIS observations of clouds in the martian mesosphere: Altitudes, wind speeds, and decameter-scale morphology

T.H. McConnochie [a,*], J.F. Bell III [b], D. Savransky [c], M.J. Wolff [d], A.D. Toigo [e], H. Wang [f], M.I. Richardson [g,h], P.R. Christensen [i]

[a] Department of Astronomy, University of Maryland, College Park, MD 20742, USA
[b] Department of Astronomy, Cornell University, Ithaca, NY 14853, USA
[c] Department of Mechanical and Aerospace Engineering, Princeton University, Princeton, NJ 08544, USA
[d] Space Science Institute, 4750 Walnut Street, Suite 205, Boulder, CO 80301, USA
[e] Applied Physics Laboratory, Johns Hopkins University, Laurel, MD 20723, USA
[f] Harvard-Smithsonian Center for Astrophysics, Cambridge, MA 02138, USA
[g] Division of Geological and Planetary Sciences, California Institute of Technology, 1200 E. California Blvd, Pasadena, CA 91125, USA
[h] Ashima Research, Pasadena, CA 91106, USA
[i] Department of Geological Sciences, Arizona State University, Tempe, AZ 85287, USA

ARTICLE INFO

Article history:
Received 21 July 2009
Revised 20 July 2010
Accepted 22 July 2010
Available online 3 August 2010

Keywords:
Mars, Atmosphere
Mars, Climate
Atmospheres, Chemistry
Atmospheres, Dynamics
Atmospheres, Structure

ABSTRACT

We present measurements of the altitude and eastward velocity component of mesospheric clouds in 35 imaging sequences acquired by the Mars Odyssey (ODY) spacecraft's Thermal Emission Imaging System visible imaging subsystem (THEMIS-VIS). We measure altitude by using the parallax drift of high-altitude features, and the velocity by exploiting the time delay in the THEMIS-VIS imaging sequence.

We observe two distinct classes of mesospheric clouds: equatorial mesospheric clouds observed between 0° and 180° L_s; and northern mid-latitude clouds observed only in twilight in the 200–300° L_s period. The equatorial mesospheric clouds are quite rare in the THEMIS-VIS data set. We have detected them in only five imaging sequences, out of a total of 2048 multi-band equatorial imaging sequences. All five fall between 20° south and 0° latitude, and between 260° and 295° east longitude. The mid-latitude mesospheric clouds are apparently much more common; for these we find 30 examples out of 210 northern winter mid-latitude twilight imaging sequences. The observed mid-latitude clouds are found, with only one exception, in the Acidalia region, but this is quite likely an artifact of the pattern of THEMIS-VIS image targeting. Comparing our THEMIS-VIS images with daily global maps generated from Mars Orbiter Camera Wide Angle (MOC-WA) images, we find some evidence that some mid-latitude mesospheric cloud features correspond to cloud features commonly observed by MOC-WA. Comparing the velocity of our mesospheric clouds with a GCM, we find good agreement for the northern mid-latitude class, but also find that the GCM fails to match the strong easterly winds measured for the equatorial clouds.

Applying a simple radiative transfer model to some of the equatorial mesospheric clouds, we find good model fits in two different imaging sequences. By using the observed radiance contrast between cloud and cloud-free regions at multiple visible-band wavelengths, these fits simultaneously constrain the optical depths and particles sizes of the clouds. The particle sizes are constrained primarily by the relative contrasts at the available wavelengths, and are found to be quite different in the two imaging sequences: r_{eff} = 0.1 μm and r_{eff} = 1.5 μm. The optical depths (constrained by the absolute contrasts) are substantial: 0.22 and 0.5, respectively. These optical depths imply a mass density that greatly exceeds the saturated mass density of water vapor at mesospheric temperatures, and so the aerosol particles are probably composed mainly of CO_2 ice. Our simple radiative transfer model is not applicable to twilight, when the mid-latitude mesospheric clouds were observed, and so we leave the properties of these clouds as a question for further work.

1. Introduction

The Mars Odyssey (ODY) spacecraft's Thermal Emission Imaging System (THEMIS) (Christensen et al., 2004) has been conducting mapping operations from Mars orbit since February 2002. Although the THEMIS investigation is directed primarily towards surface geology (*e.g.*, Christensen et al., 2005; Bandfield et al., 2004; Christensen et al., 2003; Titus et al., 2003) it routinely monitors aerosol opacities (Smith et al., 2003) with its multi-spectral infrared detector (THEMIS-IR) and images clouds and

* Corresponding author.
E-mail address: timothy.h.mcconnochie@nasa.gov (T.H. McConnochie).

0019-1035/$ - see front matter © 2010 Elsevier Inc. All rights reserved.
doi:10.1016/j.icarus.2010.07.021

dust (Inada et al., 2007) with its visible-band subsystem (THEMIS-VIS).

For a subset of the THEMIS-VIS cloud images, it is possible to discern movement of the cloud features relative to the surface. This apparent motion yields information about the altitude of the cloud, via parallax, as well information about the actual velocity of the cloud. This paper focuses on those cloud features with the largest apparent motion, which are those at mesospheric (as defined by Zurek (1992)) altitudes. At these altitudes, the apparent motion is dominated by parallax, but the eastward (*i.e.*, zonal) velocity component is also measurable.

Mesospheric clouds, and their advection by mesospheric winds, are key indicators of mesospheric dynamics and an important test for models of the martian general circulation. Furthermore, they will constrain models martian cloud microphysics, and may provide insights into the possibly analogous terrestrial phenomenon of noctilucent clouds. They might also be important for the radiative budget and chemistry of the mesosphere.

The prevailing explanation for the observed reversal in the mesosphere of the pole-to-equator temperature gradient (*e.g.*, Smith et al., 2001; Lee et al., 2009) on both Mars and Earth is that upward propagating gravity waves break in the mesosphere, thereby transporting momentum from the surface and exerting a drag on mesospheric winds (Holton, 1983; Jaquin, 1989; Joshi et al., 1995). Recent work suggests, however, that on Mars momentum transport by thermal tides is equally important (González-Galindo et al., 2009). Mesospheric condensate clouds are important for understanding the crucial momentum transport because their morphology may provide direct evidence of gravity waves, and because the wind field traced by cloud motion is of course sensitive to the amount of drag. The presence of condensate clouds also constrains the temperature field, and thus their spatial and temporal pattern of occurrence provides some insight into the mode, phase, and amplitude of the tides.

In order for clouds to form, aerosol particles must be supported by updrafts or eddy diffusion, or condensation must be rapid. Laboratory studies and models of mesospheric CO_2 cloud formation (Glandorf et al., 2002; Colaprete and Toon, 2003; Määttänen et al., 2005) imply that heterogeneous nucleation is required, unless the mesosphere is much colder than expected, and so most likely dust grains of sufficient size must be transported upward from the surface, imposing requirements on eddy diffusion and/or vertical velocities for the entire atmosphere. Similar problems exist in the study of terrestrial noctilucent clouds (*e.g.*, Kokhanovsky, 2005), which are observed in twilight and found in the summer polar mesosphere. Hunten et al. (1980) suggested meteors and micrometeors as a possible solution to the terrestrial nuclei source problem. The most significant mystery surrounding terrestrial mesospheric clouds, however, is that reports of noctilucent clouds seem to begin in the industrial era, and their frequency and latitudinal extent have shown a secular upward trend (Klostermeyer, 2002).

Jaquin (1989) suggests that martian mesospheric haze, even with a very small vertical optical depth, might be significant for the radiation budget of the poles, once the slant-path optical depth is taken into account. Clearly, however, mesospheric clouds have substantial impact on the optical depth of the mesosphere itself, and thus may significantly influence the mesosphere's ability to absorb and emit radiation. Mesospheric clouds may also impact the chemistry of the martian mesosphere. Atreya and Blamont (1990) invoke heterogeneous chemical reactions, permitted by the presence of the aerosols, to explain an observed enhancement in the rate of CO recycling back to CO_2. They suggest that a persistent depletion of CO relative to CO_2 might decrease the long term loss of CO_2 to space.

Dust, water ice, and CO_2 ice aerosols have all been observed in the martian mesosphere. Jaquin et al. (1986) and Jaquin (1988, 1989), using Viking orbiter limb imaging, reported "detached" hazes of water ice between 50 and 90 km altitudes. They also reported dust extending from the surface to as high as 50 km in most cases, although they saw dust as high as 70 km at times of exceptionally high dust loading. Clancy et al. (2007) described a class of equatorial mesospheric aerosols detected in limb observations by both the Mars Orbiter Camera (MOC) and the Thermal Emission Spectrometer (TES) solar-band bolometer on Mars Global Surveyor. These equatorial mesospheric aerosols showed a distinctive seasonal and spatial pattern, being confined to the aphelion period and most prevalent in certain longitude bands.

Nadir-pointed hyperspectral images from the Mars Express OMEGA instrument revealed distinct mesospheric clouds in these same seasons and regions that are spectroscopically identified as CO_2 ice (Montmessin et al., 2007). The altitude and velocity of these clouds can be measured directly with Mars Express's High Resolution Stereo Camera (HRSC) (Scholten et al., 2010). Määttänen et al. (2010) present a detailed analysis of the combined OMEGA and HRSC mesospheric cloud data sets, which clearly establishes the seasonal and geographical correlation of the OMEGA/HRSC mesospheric clouds with the TES/MOC limb-sounded mesospheric clouds.

Mesospheric aerosols have also been studied with solar occultation measurements performed by Phobos 2 (Chassefière et al., 1992), and more recently with solar and stellar occultation measurements by SPICAM on Mars Express (Montmessin et al., 2006a,b; Fedorova et al., 2009). These occultation measurements show evidence for both water ice (Chassefière et al., 1992; Fedorova et al., 2009) and CO_2 ice (Montmessin et al., 2006a) in the martian mesosphere.

Mesospheric clouds may have also been observed from the martian surface. On sol 39 of Mars Pathfinder lander operations, "discrete blue clouds" (Smith et al., 1997) were observed by the Imager for Mars Pathfinder (IMP) during a period from 100 to 35 min prior to sunrise. Clancy and Sandor (1998) described the same features as "discrete linear clouds" with "wave-like structure", and argued that they were directly illuminated mesospheric clouds at 80–100 km altitude and were composed of carbon dioxide ice.

The horizontally resolved images of mesospheric condensate clouds, by IMP and OMEGA, have yielded vertical optical depth (τ) estimates of $\tau \sim 0.1$ or more in the visible/near-IR (Clancy and Sandor, 1998; Montmessin et al., 2007), while the limb sounders and occultation measurements have yielded $\tau \leqslant 0.05$ (Chassefière et al., 1992; Montmessin et al., 2006a,b; Clancy et al., 2007; Fedorova et al., 2009). This difference could be a simple matter of viewing geometry, since the limb soundings and occultations are inherently an average over a large horizontal area. It could also mean that the martian mesosphere supports both diffuse condensate hazes and relatively thick discrete condensate clouds.

A wide range of particle sizes have been reported for martian mesospheric condensates. The single report by Chassefière et al. (1992) shows instances of water ice particles as small as 0.15 μm and as large as 0.9 μm effective radius. The water ice particles of Fedorova et al. (2009) are consistent with the lower end of this range at 0.1–0.3 μm. Meanwhile the Montmessin et al. (2007) CO_2 ice clouds have effective particle radii of at least 1 μm; and, in the same region, Clancy et al. (2007) give an upper limit of 1.5 μm for condensate hazes. Määttänen et al.'s (2010) detailed survey of OMEGA and HRSC mesospheric clouds agrees with the Montmessin et al. (2007) >1 μm result, but suggests that a substantial number of other cases *may* have <1 μm particles. (The authors note that detailed radiative transfer modeling of the OMEGA spectra is needed to confirm the presence of sub-micron particles.) Regarding the highest altitude mesospheric condensates, both the IMP imaging and SPICAM stellar occultations are consis-

tent with high-altitude (>80 km) CO_2 ice particles with effective radii near 0.1 μm.

Previous estimates of mesospheric zonal (east–west) winds have been made either by applying a gradient-winds methodology to temperature soundings (*e.g.*, Smith et al., 2001), or by Earth-based doppler techniques (Lellouch et al., 1991; Sonnabend et al., 2005; Moreno et al., 2009).

The gradient method is not applicable near the equator, and it requires an assumption about the surface winds as a boundary condition. The resolution of the prerequisite temperature field is also typically fairly low – 30° sampling interval in longitude and 1 scale height in altitude in the case of MGS-TES (Smith et al., 2001) – and so the wind estimate is inherently an average over large vertical and horizontal scales. The TES gradient wind estimates are available only below 0.01 millibars (about 60 km altitude), although they do have a key advantage in that they are available planet-wide in a continuous time series over a period of several martian years.

The Earth-based doppler measurements provide a more direct estimate of mesospheric wind, but with FWHM beam sizes ranging from 15% to 50% of the planet's diameter (50% for Lellouch et al. (1991), 15% for Sonnabend et al. (2005), and 20–50% for the synthesized beams of Moreno et al. (2009)), they represent averages over a broad swath of the mesosphere. (The altitude resolution is much better – Lellouch et al. (1991) and Sonnabend et al. (2005) select spectral lines confined to 60–80 km in altitude, while Moreno et al. (2009) select a line that probes 40–70 km.) Lellouch et al. (1991) use a millimeter-wave carbon monoxide absorption band and assume a functional form for the shape of the expected easterly equatorial jet in order to compensate for their poor horizontal resolution. For their single measurement near northern winter solstice, they derive an easterly speed (*i.e.*, westward flow) of 160 ± 80 m/s for the core of a jet assumed to be centered at 20° south. Sonnabend et al. (2005) find a westward (easterly) zonal flow of 74 ± 22 m/s near 20° north in mid-northern winter using a mid-infrared carbon dioxide emission line. Moreno et al. (2009) use millimeter-wave interferometry to map line-of-site winds for the full disk in a variety of martian seasons, and are able to illustrate significant diurnal variations and strong seasonal changes in the zonal winds.

In this paper we describe ∼50 measurements of altitude and velocity for mesospheric clouds that are horizontally resolved with a sampling interval of 70 m/pixel or better. In order to place the measurements in context, we compare the images with daily global maps from Mars Global Surveyor's Mars Orbiter Wide Angle Camera (MOC-WA) (Wang and Ingersoll, 2002), and we compare measured winds results from a baseline general circulation model (Richardson et al., 2007). Finally, we apply a radiative transfer model to a subset of these images in order to investigate the extent to which THEMIS-VIS can place constraints on the cloud aerosol properties.

2. Altitude–velocity measurement: theory

Apparent motion is detected as a side-effect of the THEMIS-VIS multi-spectral imaging scheme – the same location is imaged through different filters at different times, so that map-projecting the frames acquired by different filters onto the local surface will effectively co-align stationary surface features, but will create a misalignment for any feature with apparent motion caused either by parallax or velocity. A very good approximation of this parallax motion is obtained by neglecting the curvature of the planet and taking the spacecraft trajectory to be parallel to the surface. The geometry of this situation is shown in Fig. 1. Suppose that THEMIS-VIS images a cloud feature through a certain filter while the

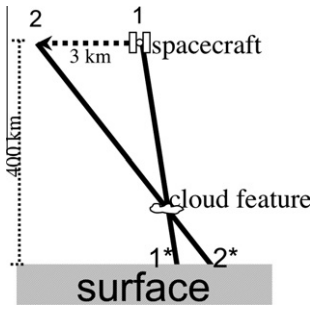

Fig. 1. Schematic (not to scale) of parallax motion. When the spacecraft moves from position 1 to position 2 between exposures, the apparent position of the cloud feature relative to the surface moves from 1* to 2*.

ODY spacecraft is at position (1), and then images the cloud feature 1 s later through another filter while the spacecraft is at position (2). The apparent position of the cloud feature relative to the surface is the intersection with the surface of a line drawn from the spacecraft through the cloud feature, and the parallax motion is the distance between the intersections of the two lines from the two different spacecraft positions. Using similar triangles we find that the parallax motion, v_{app}, is:

$$v_{app} = -v_{ODY}\frac{z_{cloud}}{z_{ODY} - z_{cloud}}, \tag{1}$$

and

$$\frac{dv_{app}}{dz_{cloud}} = -v_{ODY}\frac{z_{ODY}}{(z_{ODY} - z_{cloud})^2}. \tag{2}$$

With the ODY orbit altitude, z_{ODY}, and ground-track velocity, v_{ODY}, of approximately 400 km and 3000 m/s, a cloud at, for example, z_{cloud} = 50 km altitude has an apparent motion due to parallax of 430 m/s, and the derivative of the apparent motion is 10 m/s per km of altitude.

The THEMIS-VIS pixel sampling interval is 0.045 milliradians (Christensen et al., 2004), which amounts to 18, 36, and 72 m/pixel at the martian surface for the available 1 × 1, 2 × 2, and 4 × 4 binning modes, respectively. The narrow-band (∼50 nm FWHM) THEMIS-VIS filters are bonded directly to the surface of the detector. Each filter has a field of view of 1024 (1 × 1 binned) pixels perpendicular to the ground-track of the spacecraft ("cross-track") by 192 (1 × 1 binned) pixels parallel to the ground-track of the spacecraft ("down-track"). The orbital motion of the spacecraft causes their fields of view to pass over surface features in the following order: 869 nm, 425 nm, 654 nm, 749 nm, and 540 nm (the filters are labeled by their center wavelength). It takes slightly longer than 1 s for a surface feature to cross the down-track width of a filter, and so the delay between individual images in a THEMIS-VIS imaging sequence is set to a value close to 1 s. The interframe delay is exactly 1 s for all of the imaging sequences used in this paper. See McConnochie et al. (2006) for a more detailed discussion of THEMIS-VIS operations.

We measure apparent motion using the 425 nm ("blue") and 540 nm ("green") filters, because these filters offer the largest change in apparent pixel position for any given apparent motion. The 869 nm band is not usable due to severe stray light (McConnochie et al., 2006). The blue and green filters also offer the highest contrast for cloud features. Given the 1 s interframe delay, and the three filter widths between the blue and the green filters, most features observed in the blue filter are observed 3 s later in the green filter, and thus the 10 m/s per km of altitude of parallax motion translates to a 1.7, 0.83, or 0.42 pixels per km apparent motion in 1 × 1, 2 × 2, or 4 × 4 binned THEMIS-VIS images. Actual cloud velocity produces, of course, 0.17, 0.083, or 0.042 pixels per m/s

of apparent motion. Thus, we expect that the precision of our measurements will not be much narrower than 20 m/s in velocity and 2 km in altitude for the 4×4 binned THEMIS-VIS sequences in which most of the high-altitude clouds are detected. We also expect that, at mesospheric altitudes, the velocity motion will be much smaller than the parallax motion.

Since the parallax apparent motion is parallel to the ground track of the spacecraft (and in the opposite direction), the component of velocity parallel to the spacecraft ground track cannot be distinguished from parallax motion. Since the parallax motion is the dominant effect, this means that the ground-track parallel velocity component is essentially undetectable, and that the presence of a ground-track parallel velocity component introduces a small error in altitude which is given by Eq. (2). The Odyssey spacecraft is in a polar orbit, moving southward on the afternoon side of the orbit where all observations discussed in this paper were acquired. Thus, a 50 km high cloud feature moving southward at 50 m/s would have a measured altitude of 45 km. Meridional (north–south) winds in the martian mesosphere have never been measured, but the Joshi et al. (1995) model of gravity wave drag in the martian mesosphere leads to time-averaged meridional winds of less than 50 m/s for the regions probed by our measurements. This model calculation was for perihelion, the time of greatest meridional flow, and so a 50 m/s meridional wind can be considered an extreme case. Due to the rotation of Mars and the small inclination of the Odyssey orbit plane, the ground track is not actually due south – its heading is near 190° at mid- to low altitudes – but this introduces only a trivial (less than 2%) correction to the relationship between meridional velocity and altitude implied by Eq. (2).

2.1. Altitude–velocity measurement: method

We choose to solve for the zonal velocity, because meridional and zonal velocities are the standard basis for describing horizontal atmospheric winds, and the meridional velocity component is unresolvable as previously discussed. Fortunately, the zonal velocity is normally the dominant wind component in the atmosphere (except near the planet surface). Strictly speaking, the only velocity component that we can solve for exactly is the one perpendicular to the unknown along-track component. However, the zonal velocity component is nearly perpendicular, and so the error introduced by the unresolved along-track wind component is small – <10 m/s for the extreme case of 50 m/s along-track winds, which is comparable to other systematic errors (see below).

Figs. 2–5 illustrate our method using a particular measurement from THEMIS-VIS image sequence V04573003 as an example. Fig. 2 shows a contour plot of the correlation of the blue filter image with the green filter image as a function of zonal (eastward) velocity and altitude above the Mars reference ellipsoid. Fig. 3 shows the region of the V04573003 Reduced Data Record (RDR) used to calculate the correlation (described below), which we will henceforth refer to as the correlation region of interest (“correlation-ROI”). Fig. 4 shows the blue filter projected onto the green filter correlation-ROI at the best fit (maximum correlation) altitude and velocity, and Fig. 5 shows the same projection using the altitude and velocity (zero by definition) of the local surface.

All of our measurements are performed using THEMIS-VIS RDRs, which are available from NASA’s Planetary Data System. Each RDR contains all of the filter images from all of the exposures in a THEMIS-VIS imaging sequence. Each plane of the RDR stores all the individual filter images for a given filter, arranged in temporal order. We refer to these individual filter images as “framelets”. Each framelet is a 1024 by 192 (or 512 by 96 or 256 by 48 for 2×2 or 4×4 binning) array of radiance values for a single filter in a single exposure. (See McConnochie et al. (2006) for the details of RDR layout and radiance calibration.) The correlation-ROI is defined as a rectangular region within the green filter plane of the RDR. Normally, this region encompasses multiple framelets, and so when the correlation-ROI is displayed without map projection there are discontinuities at the framelet boundaries, as seen in Fig. 4.

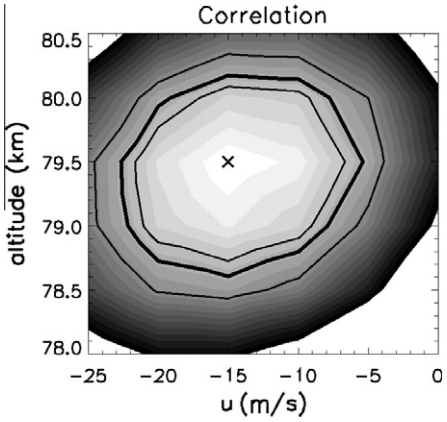

Fig. 2. Correlation as a function of altitude and zonal velocity. The shaded contours show the difference between the correlation and the peak correlation (indicated by “X”), with contours at intervals of 0.25 in units of the standard error of the correlation. The black lines show a test of the hypothesis that the correlation at a given grid point is not less than the maximum correlation. The thick black line shows the 5% level for this hypothesis, which defines our confidence intervals. The outer and inner thin black lines show the 1% and 10% levels, respectively.

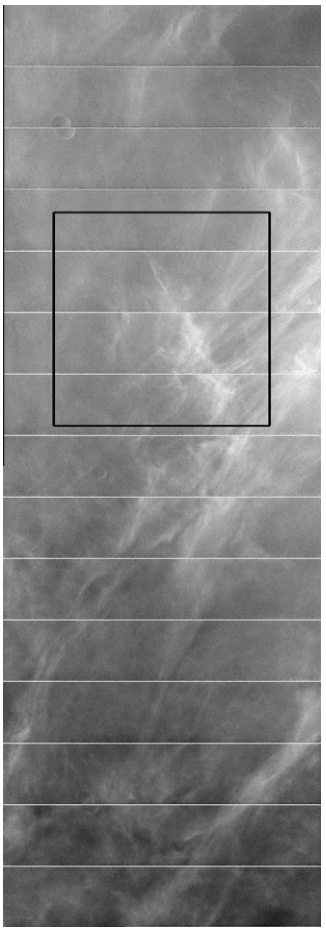

Fig. 3. The V04573003c ROI, which is used to generate the correlation map shown in Fig. 2.

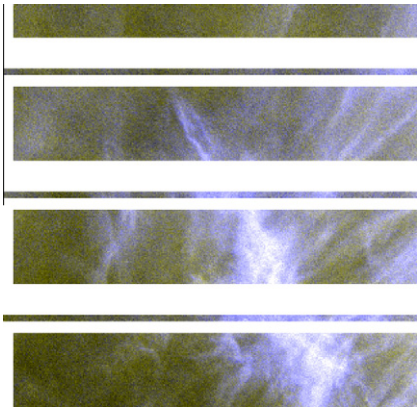

Fig. 4. Co-alignment of the green and blue filters at the best-fit altitude and velocity solution for the V04573003c ROI. The blue filter has been projected onto the green filter RDR as described in the text. In this figure, regions of the ROI that are invalid for calculating the correlation according to the criteria described in the text are left blank. The red and green channels of this RGB figure are controlled by the green filter ROI image, and the blue channel by the projected blue filter image. Each filter is stretched individually to maximize contrast. (For interpretation of the references to color in this figure legend, the reader is referred to the web version of this article.)

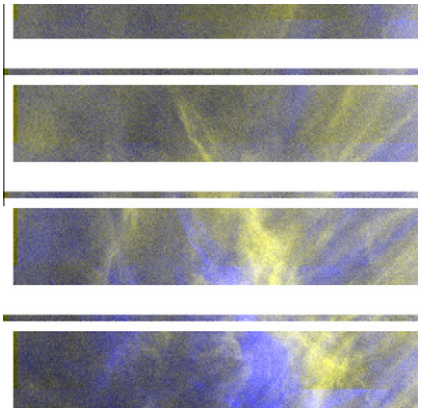

Fig. 5. Co-alignment (*i.e.*, lack thereof) of the green and blue filters at the altitude of the local surface for the V04573003c ROI. Otherwise the same as Fig. 4. (For interpretation of the references to color in this figure legend, the reader is referred to the web version of this article.)

To calculate the correlation, we first classify each RDR pixel as either valid or "null" (invalid). Valid pixels are used for calculating the correlation, and null pixels are excluded. The valid region of the framelets is defined so as to exclude the regions which commonly contain stray light artifacts (cf. McConnochie et al., 2006). In framelet coordinates, the valid region is samples 160–840, lines 0–176 for 1×1 binning (divide these coordinates by 2 or 4 for 2×2 or 4×4 binning, respectively). Framelet line-sample coordinates are the same as the line and sample numbers in the RDR, except for a translation setting the lowest line number in a framelet equal to 0. All pixels outside the valid region in a framelet are set to null. Pixels that are null in the original RDR are also classified as null.

Next, we project the blue filter data onto the green filter correlation-ROI with the given assumed altitude and velocity. To do so, we handle each green filter framelet within the correlation-ROI separately, and perform the following steps:

1. Calculate the latitude and longitude of each pixel in all blue filter framelets near to the green filter correlation-ROI. We do so following the method of the Unites States Geological Survey's ISIS software package (Torson and Becker, 1997; Gaddis et al., 1997, http://isis.astrogeology.usgs.gov/), which we have adapted to apply to targets of arbitrary altitude. This method consists of:
   (a) use the NASA Navigation and Ancillary Information Facility's SPICE data kernels and toolkit (Acton, 1996) to determine the exact position and attitude of ODY with respect to Mars, and from that the boresight vector of the THEMIS-VIS instrument;
   (b) use the ISIS package's THEMIS-VIS camera model, which includes a correction for optical distortion, to derive the pointing vector for each pixel from the boresight vector;
   (c) identify latitude and longitude of each pixel as the intersection of its pointing vector with an ellipsoid parallel to the Mars reference ellipsoid and at a given altitude above it.

   To verify this latitude and longitude calculation method, we have used it to map project THEMIS-VIS framelets from all filters onto the local surface elevation. These map projection tests show that we obtain results identical to the ISIS software. They also show occasional misalignment of surface features by up to two 1×1 binning pixels. This means that inaccuracies in the ISIS camera model, or, less likely, the SPICE data kernels, may cause systematic errors in our altitude and velocity measurements of up to 1 km in altitude or 10 m/s in velocity. These potential errors are comparable to the systematic errors introduced by the possibility of non-zero meridional velocity. They are in almost all cases smaller (but not dramatically so) than the width of the statistical confidence intervals of the cross-correlation solution. We have not pursued this issue further; doing so may be of some modest value to future work.
2. Adjust the longitude of each blue filter pixel to compensate for the assumed zonal velocity. The necessary translation for the given velocity depends on the time elapsed between the green filter framelet and each blue filter framelet, and the result of the translation is that locations in the blue filter framelet are labeled with longitudes projected forward to the time that the green filter framelet was exposed.
3. Convert the latitude and velocity compensated longitude for each blue filter framelet pixel into a line and sample number in the reference frame of the green filter framelet's framelet coordinates. Our method in this step is also based on the ISIS software package:
   (a) calculate the vector from ODY to a pixel's latitude and compensated longitude on the ellipsoid at the given altitude;
   (b) apply the inverse of the ISIS package's THEMIS-VIS camera model to determine the sample and line number referenced to the green filter framelet's origin.
4. Interpolate the blue filter framelet image from the non-integer line and sample coordinates calculated for the blue filter pixels in the preceding step to the integer line-sample coordinates of the green filter framelet. We perform a separate linear interpolation for each blue filter framelet onto the green filter framelet. Interpolated values are only created in the interior of each region covered by valid blue filter framelet pixels. Any pixels of the interpolated blue filter image which are interior to none of these regions are classified as null.

The above procedure results in a blue filter image that has been projected onto the green filter image for each framelet in the correlation-ROI. We then assemble these projected blue filter framelets into the blue filter projected image of the correlation-ROI. Any pixel which is null in either the projected blue filter correlation-ROI or the original green filter correlation-ROI is now set to null in both. Figs. 4 and 5 are examples of the green filter correlation-ROI overlain with the projected blue filter correlation-ROI. Null pixels are blank (white) in these figures.

Electron counting noise in the image pixels leads to noise at a characteristic frequency in maps of correlation versus altitude and velocity. To address this, we apply a gaussian smoothing function, with a FWHM of 3 pixels in both the line and sample direction, to both the green filter and projected blue filter correlation-ROI images prior to calculating the correlation. We observe, *e.g.*, Fig. 2, that this smoothing eliminates the noise in the correlation map and improves the overall precision of the measurement.

The altitude and velocity for the correlation-ROI are those that give the highest correlation between the projected blue filter and the green filter correlation-ROI. To find the maximum correlation, we first apply a downhill simplex non-linear optimization routine based on the "amoeba" routine from Press et al. (1992). Our modified amoeba search halts when the change in altitude and velocity with subsequent iterations is less 0.5 km in altitude and 5 m/s in velocity. We then perform an adaptive grid search on the altitude–velocity space surrounding the best fit produced by the amoeba search. The adaptive grid search allows us to map the probability density function of the altitude and velocity fit and acts as a consistency check for the amoeba search results. Our reported "best-fit" altitude and velocity estimate is the grid point with maximum correlation.

For the grid search, all grid points on the boundary of the grid must have a correlation more than three standard errors below that of the grid point with the best correlation. If this criterion is not satisfied for a particular boundary, the grid is expanded in that direction until it is satisfied. This adaptive grid search is performed up to three times with the grid sampling intervals decreased by a factor of two after each iteration. The initial grid sampling intervals are 2 km in altitude and 20 m/s in velocity. If the size of the adapted grid at the end of an iteration is larger than 10 grid points in either dimension, the grid search is halted in order to conserve computational resources.

One problem inherent in this correlation search method, as in all real-world localization problems, is that the movement of significant image features into or out of the region of interest as the altitude or velocity is changed leads to spurious changes in the correlation. For example, surface features are often visible beneath the high-altitude cloud features that we are correlating. As the altitude and velocity are adjusted, a surface could move out of the region of valid pixels, artificially improving the calculated correlation. We mitigate this problem in two ways.

1. When performing the grid search, we require the correlation calculation at every grid point in an iteration to use the same set of correlation-ROI pixels. Effectively, we set all pixels that are null at any grid point to be null at all grid points. For the wider range of velocities and altitudes considered by the amoeba search, this strict pixel validity requirement is infeasible, because it would lead to the majority of pixels being labeled null. The amoeba search therefore begins to use the strict pixel validity requirement only after it has narrowed down the altitude and velocity range. Once the amoeba search is altering the altitude and velocity estimates by less than 4 km and 40 m/s per iteration, it switches to the strict pixel validity requirement. For the amoeba search the validity requirement is cumulative once the strict requirement is invoked. Pixels that were invalid in one correlation calculation remain invalid for all future correlation calculations.
2. We project, as previously discussed, the blue filter framelets onto the green filter, instead of the other way around. The above strict pixel validity requirement prevents any change in the features of the unprojected filter that are used in the correlation. However, it does not prevent features in the projected filter from moving into and out of the correlation-ROI. Surface features visible though the high-altitude cloud are much more prominent in the green filter than the blue filter. Thus, by using the blue filter as the projected filter, we minimize the significance of surface features causing spurious changes in the correlation by moving into or out of the correlation-ROI.

To calculate the standard error of the correlation coefficients at each grid point, we apply the bootstrap method (Efron and Tibshirani, 1993) at the grid point with the highest correlation. This bootstrap calculation generates 1000 simulated data sets by randomly sampling, with replacement, from the valid points in the correlation-ROI. The number of points in each simulated data set is equal to the number of points in the correlation-ROI. It then calculates the correlation for each simulated data set, generating a set of correlation measurements that simulates repeating the correlation measurement 1000 times. The bootstrap standard error is the standard deviation of this simulated correlation data set. To identify the confidence intervals for the altitude and velocity estimates, we construct a test of the hypothesis that the correlation at a given grid point is not less than the maximum correlation, using the bootstrap standard error as the standard error for both the maximum correlation and the grid points. Our reported confidence intervals contain all points for which the probability of this hypothesis is greater than 5%. In Fig. 2, the boundaries of this confidence interval are illustrated by a bold black line.

2.2. Altitude–velocity measurement: candidate selection

We have found that the most efficient and reliable method of identifying candidate mesospheric clouds in the THEMIS-VIS data set is to visually inspect each multi-spectral THEMIS-VIS image. Important obstacles to doing this automatically are: (1) false positives caused by calibration artifacts and/or very low contrast image features; and (2) false negatives caused by the proximity of surface features to mesospheric cloud features.

We perform the search for candidates by map-projecting all multi-spectral THEMIS-VIS images onto the local surface and assembling the filters into enhanced color renderings such as those in Fig. 6. The enhanced color rendering simply assigns the blue, green, and "red" (654 nm) filter images to the blue, green and red channels of the standard RGB color space, stretching each filter image individually so that $\pm\alpha$ standard deviations from its mean fills the full dynamic range of the corresponding channel. If the "red" (654 nm) filter is not present in a given image sequence, the 749 nm filter is used in its place. We chose α on a case by case basis, but typically use $\alpha = 2$. Any apparent motion relative to the surface shows up as a misalignment between the color channels. We rely on this misalignment to identify the mesospheric cloud candidates.

THEMIS-VIS sequence V04573003 (see Fig. 6) was the first misalignment identified in the data set. Prior to its discovery, there was no expectation that mesospheric clouds would be observable by THEMIS-VIS. To date we have examined all multi-spectral THEMIS-VIS image sequences up to and including sequence V18086011 (acquired January 11, 2006). Whenever an apparent color misalignment is identified, we then select one or more correlation-ROIs from the RDR of that imaging sequence. The rectangular correlation-ROIs are selected to enclose a region of morphologically similar misaligned features while avoiding, as much as possible, high contrast surface features. When the misaligned features cover a large portion of the sequence, or when there are multiple morphologically distinct groups of apparent high-altitude clouds, we select multiple correlation-ROIs in that sequence. We have also selected a few cloud features with no apparent misalignment to serve as a control for our identification method. Tables 1–4 list all of the candidate correlation-ROIs, including the controls.

The selected candidate correlation-ROIs range from cases of obvious cloud features with dramatic misalignment, to cases with

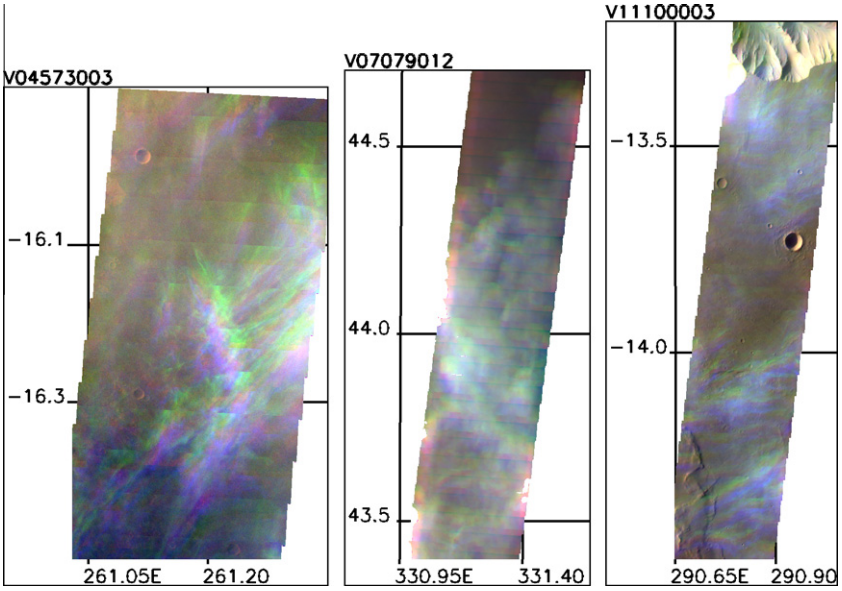

Fig. 6. Example discovery images, showing the appearance of mesospheric clouds when map projected using the altitude of the local surface. These images use enhanced color rendering defined in the text, the grid lines give degrees east longitude and degrees north latitude, and the projection is sinusoidal. (For interpretation of the references to color in this figure legend, the reader is referred to the web version of this article.)

Table 1
Correlation-ROIs: equatorial mesospheric cloud candidates.

ID[a]	L_s	N. Lat.[b]	E. Lon.[b]	Inc.[b] (°)	Samples[c]	Lines[c]
V04573003a	113.7	−16.661	261.136	80.2	59–421	1164–1398
V04573003b	113.7	−16.410	261.172	80.1	94–433	687–936
V04573003c	113.7	−16.240	261.196	80.0	84–420	322–655
V10324001a	18.3	−5.003	356.963	67.9	117–440	1263–1644
V10526009a	26.1	0.523	261.881	68.9	86–429	713–1126
V11100003a	47.5	−14.359	290.794	78.0	76–217	4685–4894
V11100003b	47.5	−14.071	290.818	77.9	44–203	4393–4639
V11100003c	47.5	−13.562	290.891	77.8	53–220	3918–4151
V12922001a	113.8	−6.201	292.486	83.0	101–334	268–658
V13072001a	119.6	−5.308	285.542	82.9	80–257	1194–1333
V13072001b	119.6	−5.208	285.576	82.9	67–341	802–1354

[a] THEMIS-VIS sequence number, with a lower case letter appended to distinguish individual ROIs.
[b] At the center of the ROI.
[c] Line/sample numbers as stored in RDR; first sample, line labeled 0, 0.

Table 2
Correlation-ROIs: northern winter mesospheric cloud candidates L_s = 200–250°.

ID[a]	L_s	N. Lat.[b]	E. Lon.[b]	Inc.[b] (°)	Samples[c]	Lines[c]
V06705017a	206.1	49.723	318.187	94.9	41–217	1067–1621
V06717019a	206.7	51.174	332.432	95.4	22–226	67–418
V06768014a	209.3	44.059	300.252	94.1	30–223	536–894
V06768014b	209.3	44.369	300.311	94.2	29–230	311–523
V06768014c	209.3	44.622	300.359	94.2	26–232	51–299
V06793016a	210.5	40.500	298.631	93.3	41–228	2296–2891
V06793016b	210.5	42.161	298.929	93.8	25–224	691–1305
V06905017a	216.2	45.794	309.566	96.1	24–224	3000–3338
V06905017b	216.2	46.597	309.723	96.4	26–224	2216–2574
V06917014a	216.8	44.586	323.246	95.8	47–211	678–935
V06930045a	217.4	44.660	308.360	96.0	40–218	4148–4599
V06930045b	217.4	45.830	308.585	96.4	42–221	2921–3574
V06930045c	217.4	47.637	308.944	97.0	36–222	1354–1666
V07005019a	221.3	43.785	305.275	96.4	31–230	527–974
V07005019b	221.3	44.324	305.377	96.6	35–222	34–424
V07029045a	222.5	46.433	333.637	97.5	38–215	3040–3438
V07029045b	222.5	48.225	333.997	98.2	36–214	1380–1650
V07067015a	224.4	44.425	317.417	97.1	41–213	2616–2867
V07079012a	225.0	42.557	330.996	96.5	32–209	4287–4671
V07079012b	225.0	42.986	331.075	96.7	31–217	3865–4259
V07079012c	225.0	43.848	331.234	97.0	34–223	3042–3430
V07079012d	225.0	44.416	331.342	97.2	33–224	2433–2942
V07080012a	225.1	42.730	302.198	96.6	39–212	2671–2969
V07080012b	225.1	44.117	302.479	97.1	36–219	1273–1704
V07105019a	226.4	41.141	300.979	96.2	50–209	3150–3376
V07105019b	226.4	41.700	301.072	96.4	48–201	2553–2900
V07166022a	229.5	39.663	341.549	95.9	47–202	3779–4009
V07166022b	229.5	40.575	341.708	96.3	48–202	2891–3144
V07166022c	229.5	41.855	341.928	96.8	54–194	1638–1939
V07166022d	229.5	43.457	342.231	97.4	41–214	79–411
V07467019a	245.2	48.212	302.699	100.5	39–213	730–1138
V07504020a	247.1	46.357	315.269	99.7	44–208	1160–1385

[a] THEMIS-VIS sequence number, with a lower case letter appended to distinguish individual ROIs.
[b] At the center of the ROI.
[c] Line/sample numbers as stored in RDR; first sample, line labeled 0, 0.

barely visible features and questionable misalignment. Even though we take care to include marginal cases as candidates, this detection method is obviously biased towards the highest altitude clouds. This is one reason why we have chosen to limit this work to mesospheric clouds. Even though our measurement technique is precise enough to detect the altitude of lower atmosphere clouds, the misalignment is too small to be noted by visual inspection. In fact, some of the control correlation-ROIs yield altitudes in the ~10 km range (none exceeded 13 km). It may ultimately be feasible to define correlation-ROIs for all cloud features in the THEMIS-VIS data set, but reliably distinguishing low-altitude clouds from surface features will be problematic, especially when the signal is very low as it often is in winter mid-latitudes. Since such an effort would be expensive in terms of both human time and computer time, we have decided that it is beyond the scope of this work. Thus we restrict ourselves to 40+ km altitudes in order to ensure that we have a nearly complete census.

In order to decide whether our correlation algorithm has successfully identified a cloud's altitude and velocity we look at the width of the confidence interval for the altitude solution. In some cases, the algorithm will give a non-zero altitude–velocity solution for which visual inspection shows no improvement in the co-alignment of what were believed to be the cloud features. These algorithm failures appear to be caused by calibration artifacts in the THEMIS-VIS images (see McConnochie et al., 2006), which will

Table 3
Correlation-ROIs: northern winter mesospheric cloud candidates L_s = 250–300°.

ID[a]	L_s	N. Lat.[b]	E. Lon.[b]	Inc.[b] (°)	Samples[c]	Lines[c]
V07804021a	262.8	40.115	302.462	95.6	36–206	2573–2901
V07804021b	262.8	38.696	302.218	94.9	34–220	3856–4343
V07829020a	264.1	47.187	302.854	99.3	43–206	3011–3608
V07829020b	264.1	48.250	303.066	99.8	41–210	2166–2411
V07890023a	267.2	41.708	342.524	95.8	33–212	2326–2701
V07941020a	269.9	44.094	312.117	96.7	37–216	2662–2989
V07941020b	269.9	45.354	312.350	97.4	38–218	1462–1764
V07954018a	270.6	40.326	296.543	94.5	40–214	2986–3474
V08028019a	274.4	43.697	322.877	95.6	47–203	3090–3563
V08028019b	274.4	44.219	322.975	95.9	43–208	2556–3090
V08057021a	275.9	38.986	205.726	92.7	40–209	529–855
V08140022a	280.1	42.678	332.560	93.9	46–202	2123–2484
V08140022b	280.1	44.092	332.820	94.7	43–211	695–1190
V08141026a	280.2	41.550	303.553	93.2	18–232	1140–1418
V08141026b	280.2	42.297	303.684	93.7	51–221	437–685
V08165025a	281.4	44.069	331.810	94.4	42–208	830–1528
V08165025b	281.4	45.069	331.999	95.0	43–211	69–362
V08166020a	281.5	42.530	302.725	93.5	38–207	215–568
V08178017a	282.1	53.987	318.934	99.9	38–216	683–989
V08266019a	286.5	45.988	299.321	94.3	42–212	2503–2769
V08266019b	286.5	46.449	299.402	94.6	44–202	2020–2366
V08266019c	286.5	46.922	299.494	94.9	40–204	1595–1881
V08266019d	286.5	47.454	299.604	95.2	36–217	934–1516
V08266019e	286.5	48.116	299.733	95.5	36–209	372–800
V08278020a	287.2	48.334	313.667	95.5	23–225	1168–1508
V08278020b	287.2	49.130	313.828	96.0	23–221	351–791
V08290017a	287.8	44.911	326.900	93.4	40–212	492–992
V08302017a	288.4	46.826	341.161	94.3	46–210	645–1131
V08302017b	288.4	47.426	341.275	94.7	48–207	28–591
V08303022a	288.4	49.074	312.783	95.6	24–226	2800–3328
V08303022b	288.4	51.293	313.244	96.9	28–221	576–1276
V08428013a	294.7	50.802	308.871	95.0	33–215	4101–5054
V08428013b	294.7	52.979	309.343	96.3	36–218	2176–2773
V08503016a	298.4	48.700	305.923	92.8	49–211	2935–3375
V08503016b	298.4	49.495	306.085	93.3	50–212	2119–2658

[a] THEMIS-VIS sequence number, with a lower case letter appended to distinguish individual ROIs.
[b] At the center of the ROI.
[c] Line/sample numbers as stored in RDR; first sample, line labeled 0, 0.

Table 4
Correlation-ROIs: controls.

ID[a]	L_s	N. Lat.[b]	E. Lon.[b]	Inc.[b] (°)	Samples[c]	Lines[c]
V08806011a	313.1	29.804	203.173	78.0	41–213	2628–3104
V09543022a	346.5	32.091	182.502	71.7	29–213	1069–1465
V09550015a	346.8	43.752	342.489	76.5	39–211	1247–1509
V09575016a	347.8	48.573	342.225	78.3	37–220	852–1189
V09912021a	1.9	52.484	341.718	76.2	40–211	809–1184

[a] THEMIS-VIS sequence number, with a lower case letter appended to distinguish individual ROIs.
[b] At the center of the ROI.
[c] Line/sample numbers as stored in RDR; first sample, line labeled 0, 0.

dominate scene cross-correlation if the cloud contrast is very low or nonexistent. However, we invariably find these apparent algorithm failures to have confidence intervals wider than 10 km in altitude, and so we chose at 10 km as our cutoff in order to eliminate false positives.

3. Altitude–velocity results

In Table 5–8 we show results from all correlation-ROIs that yield altitudes greater than 40 km and have confidence intervals less than 10 km wide. Each result is given an ID which consists of the THEMIS-VIS sequence number followed by a lower case letter specifying the ROI. All of the observed mesospheric clouds fall into one of two distinct classes: equatorial clouds observed in the solar longitude (L_s) range 0–180°, listed in Table 5, and northern mid-latitude clouds observed in L_s = 200–300°, listed in Tables 6–8. The northern mid-latitude clouds are organized into subclasses by our assessment of their morphology. Table 6 shows the "clumpy" subclass, which consists of any cloud that shows extensive small scale structure but no obvious larger scale organization. In Table 7 we list "linear" clouds, those that are organized into one or more southwest-to-northeast trending linear features. The final northern mid-latitude subclass, listed in Table 8, consists of "linear periodic" clouds, those whose multiple linear features show regular spacing. The equatorial mesospheric clouds also show some morphological diversity. Three of them, V04573003, V10526009, and V11100003 show long narrow filamentary structures, while the other two do not. Example map projected images from both classes and each subclass are shown in Figs. 7–10.

3.1. Description of the atmospheric global circulation model (GCM) used for comparison with observed winds

In order to put our equatorial velocity measurements into context, we have compared them with a martian atmospheric general circulation model (GCM), "MarsWRF" (Richardson et al., 2007). MarsWRF uses a terrain-following, hydrostatic pressure ("eta") vertical coordinate, with the top layer of the model located at about 100 km above the reference geoid. To represent the diurnal and seasonal heating radiative heating rates, a prescribed dust opacity distribution that simulates the first year of Mars Global Surveyor mapping operations is used. (This is identical to the Mars Climate Database "MGS scenario" for dust described by Lewis et al. (1999).) This year (see Smith, 2004) can be considered typical of years without a planet encircling dust storm. No such planet-encircling storm occurred in the year that contains our mid-latitude cloud observations, and the equatorial cloud observations occur in seasons where interannual dust variability is not a major factor. (The possibility of smaller scale dust storms must still be considered when interpreting our mid-latitude observations.) The MarsWRF simulation we have used uses the hydrostatic approximation, has a spatial resolution of ° in latitude and longitude (approximately 120 km between grid points), and has 40 vertical layers with a typical thickness of approximately 3 km in the mesosphere. Output from the simulation was recorded every 2 h of model integration time (*i.e.*, 12 values per sol).

All Mars GCMs include some form of damping near their model tops to parameterize gravity wave drag. MarsWRF uses Rayleigh drag, the most common form of simple momentum and temperature damping. It spreads the damping over the three uppermost model layers, which have damping time constants, from highest to lowest, of 2, 6, and 18 sols. The altitude of the lowest Rayleigh drag level ranges from ~75 km (in the aphelion season) to ~85 km (in northern fall and winter). This form of gravity wave drag parameterization is not optimized for accuracy in the upper GCM layers; its main purpose is to prevent gravity waves from reflecting off the top of the model and influencing the lower layers that have historically been most readily compared with observations. Since direct measurements of winds are scarce at any altitude on Mars, it is difficult to match a GCM to the wind field. Our chosen model does a good job of representing the observed mean zonal temperature structure, and so it produces mean zonal flows consistent with the thermal winds that can be inferred from these temperature observations. Thus, the model represents a reasonable point of comparison with our wind measurements, but we must keep in mind the limitations of the model, especially the altitude region in which the wind measurements were taken and the lack of comprehensive wind data against which to validate this (or any other) model.

Table 5
Altitude and velocity measurements: equatorial.

ID	L_s (°)	N. Lat. (°)	E. Lon. (°)	Local solar time (h)	Inc. angle (°)	Measured				MarsWRF GCM	
						Altitude (km)		Zonal velocity (m/s)		Zonal velocity (m/s)	
						Best fit	Conf. interval	Best fit	Conf. interval	Mean	±2σ
V04573003a	114	−17	261	16.8	80.2	79.5	79.0–80.0	−15	−20 to −10	−9	−35 to 16
V04573003b	114	−16	261	16.8	80.1	80.0	79.0–81.0	−5	−15 to 0	−9	−35 to 16
V04573003c	114	−16	261	16.8	80.0	80.0	79.5–80.5	−5	−5 to 0	−10	−37 to 17
V10526009a	26	1	262	16.6	68.9	74.0	71.5–76.0	−90	−110 to −70	−38	−65 to −11
V11100003a	48	−14	291	16.8	78.0	61.0	59.5–62.0	−65	−80 to −50	−8	−33 to 17
V11100003b	48	−14	291	16.8	77.9	61.5	61.0–62.5	−50	−60 to −35	−9	−35 to 17
V11100003c	48	−14	291	16.8	77.8	62.0	61.0–63.5	−65	−80 to −45	−9	−35 to 16
V12922001a	114	−6	292	17.3	83.0	57.0	56.5–57.5	−45	−50 to −40	−4	−20 to 12
V13072001a	120	−5	286	17.3	82.9	60.0	58.5–61.0	−45	−60 to −30	−19	−41 to 3
V13072001b	120	−5	286	17.3	82.9	59.0	57.5–60.5	−70	−85 to −55	−9	−39 to 21

Note: L_s, Lat., and Lon. coordinates have been rounded to save space.

Table 6
Altitude and velocity measurements: mid-latitude, "clumpy" class.

ID	L_s (°)	N. Lat. (°)	E. Lon. (°)	Local solar time (h)	Inc. angle (°)	Measured				MarsWRF GCM	
						Altitude (km)		Zonal velocity (m/s)		Zonal velocity (m/s)	
						Best fit	Conf. interval	Best fit	Conf. interval	Mean	±2σ
V06768014a	209	44	300	17.6	94.1	52.5	50.5–54.5	85	65–100	51	19–84
V06793016b	211	42	299	17.6	93.8	48.5	47.0–49.5	75	65–90	67	33–102
V06905017a	216	46	310	17.6	96.1	62.0	60.0–63.5	60	45–80	74	27–122
V06905017b	216	47	310	17.6	96.4	61.0	59.5–62.0	65	50–80	69	29–108
V06930045b	217	46	309	17.6	96.4	70.0	68.5–72.0	65	50–75	98	68–128
V06930045c	217	48	309	17.6	97.0	73.5	71.5–75.0	75	60–90	94	57–132
V07005019a	221	44	305	17.5	96.4	64.0	62.5–65.5	25	10–35	82	34–130
V07005019b	221	44	305	17.5	96.6	65.0	63.5–67.0	35	25–50	86	43–129
V07029045a	223	46	334	17.5	97.5	63.0	60.5–65.5	40	20–55	68	41–95
V07079012a	225	43	331	17.5	96.5	70.5	69.0–72.0	0	−10 to 10	91	39–143
V07079012b	225	43	331	17.5	96.7	69.5	68.5–70.5	0	−10 to 5	91	38–143
V07079012c	225	44	331	17.5	97.0	68.0	67.0–69.0	−10	−20 to −5	80	32–128
V07079012d	225	44	331	17.5	97.2	69.5	68.5–70.5	25	20–30	94	94–142
V07105019b	226	42	301	17.5	96.4	70.0	65.0–74.0	−30	−70 to 5	89	62–116
V07166022c	230	42	342	17.5	96.8	60.0	55.0–64.0	50	20–80	70	49–90
V07166022d	230	43	342	17.5	97.4	59.0	57.0–61.5	55	35–70	70	48–91
V07804021a	263	40	302	17.0	95.6	51.5	51.0–52.0	30	25–35	12	−4 to 28
V07804021b	263	39	302	17.0	94.9	54.0	53.0–54.5	15	10–25	7	−10 to 23
V07941020a	270	44	312	16.9	96.7	49.0	47.5–50.0	35	25–45	42	13 –71
V07941020b	270	45	312	16.9	97.4	49.5	47.0–51.5	30	15–45	52	23–81
V07954018a	271	40	297	16.9	94.5	52.5	51.0–53.0	0	−10 to 10	33	−16 to 83
V08140022a	280	42	333	16.7	93.9	49.5	48.0–51.5	60	45–75	48	18–78
V08140022b	280	44	333	16.7	94.7	48.0	46.0–50.0	60	50–75	54	16–92
V08266019a	287	46	299	16.6	94.3	49.5	46.5–52.0	50	30–75	57	16–99
V08266019b	287	46	299	16.7	94.6	50.5	49.0–52.0	35	20–50	61	23–99
V08266019c	287	47	299	16.7	94.9	51.5	49.5–53.0	40	20–60	55	14–96
V08266019d	287	47	300	16.7	95.2	47.0	45.0–49.0	45	25–60	72	31–113
V08278020a	287	48	314	16.7	95.5	47.0	45.5–48.5	120	105–130	79	31–127
V08278020b	287	49	314	16.7	96.0	47.0	46.0–48.5	120	105–130	87	48–126

Note: L_s, Lat., and Lon. coordinates have been rounded to save space.

To make the wind velocity comparisons, we use the final year of the 10-year simulation and select the vertical level closest to the measured altitude of the given mesospheric cloud. The closest model level is always within 1.2 km (about 1/6 of a scale height at these altitudes) of the mesospheric cloud altitude. We then select the four model grid points closest to the latitude–longitude coordinates of the mesospheric cloud from each of the two local times nearest to that of the cloud image, and from each of four days surrounding the L_s of the cloud image. We use all of these points to generate the mean and standard deviation of the model winds shown in Tables 5–8.

3.2. Equatorial mesospheric clouds

The equatorial mesospheric clouds were discovered by pure chance in images targeted at surface features. Fig. 11 shows the spatial distribution of these equatorial clouds, comparing it with the distribution of all THEMIS-VIS image sequences that "could have detected" mesospheric clouds had they been present. To detect mesospheric clouds, a THEMIS-VIS image sequence must obviously be multi-spectral. In addition, for purposes of Fig. 11, we have also excluded types of image sequences which we believe are substantially less likely to detect mesospheric clouds. These are: (1) images that do not have both the green and blue filters, since these filters provide much better contrast for cloud features; (2) 1 × 1 binning sequences, since the spatial coverage of an individual 1 × 1 sequence is very small; (3) short exposure times (<1 ms for 2 × 2 binning or 0.5 ms for 4 × 4 binning), since such sequences have serious stray light problems that tend to obscure subtle features; (4) incidence angles >90°, since these tend to have low signal levels.

Out of the 2048 could-have-detected sequences plotted in the lower panel of Fig. 11, we have found five with equatorial meso-

Table 7
Altitude and velocity measurements: mid-latitude, "linear" class.

ID	L_s (°)	N. Lat. (°)	E. Lon. (°)	Local solar time (h)	Inc. angle (°)	Measured				MarsWRF GCM	
						Altitude (km)		Zonal velocity (m/s)		Zonal velocity (m/s)	
						Best fit	Conf. interval	Best fit	Conf. interval	Mean	±2σ
V06705017a	206	50	318	16.6	94.9	50.0	48.0–52.0	85	60–105	79	46–111
V06793016a	211	41	299	17.6	93.3	47.5	46.0–49.5	55	35–75	63	39–88
V07467019a	245	48	303	17.3	100.5	44.5	43.5–46.0	95	80–105	84	43–126
V07829020b	264	48	303	17.1	99.8	41.0	38.0–43.5	50	15–90	60	40–79
V08028019a	274	44	323	16.8	95.6	60.0	56.5–61.0	25	−10 to 55	54	9–98
V08028019b	274	44	323	16.8	95.9	50.5	47.5–51.5	50	25–75	44	−20 to 108
V08057021a	276	39	206	16.8	92.7	46.5	43.5–51.0	35	10–75	15	−18 to 48
V08302017a	288	47	341	16.6	94.3	50.5	47.5–54.0	55	20–80	62	45–80
V08302017b	288	47	341	16.6	94.7	46.5	43.5–48.0	85	65–110	74	53–94
V08303022a	288	49	313	16.6	95.6	46.0	45.0–47.5	110	100–120	91	60–122
V08503016b	298	49	306	16.5	93.3	45.0	44.5–46.0	60	45–70	93	57–129

Note: L_s, Lat., and Lon. coordinates have been rounded to save space.

Table 8
Altitude and velocity measurements: mid-latitude, "linear periodic" class.

ID	L_s (°)	N. Lat. (°)	E. Lon. (°)	Local solar time (h)	Inc. angle (°)	Measured				MarsWRF GCM	
						Altitude (km)		Zonal velocity (m/s)		Zonal velocity (m/s)	
						Best fit	Conf. interval	Best fit	Conf. interval	Mean	±2σ
V07890023a	267	42	343	17.0	95.8	54.0	51.0–56.0	30	10–50	43	13–72
V08141026a	280	42	304	16.7	93.2	51.5	48.5–53.0	70	50–85	41	19–63
V08141026b	280	42	304	16.7	93.7	52.5	50.5–54.5	55	40–70	39	15–64
V08165025b	281	45	332	16.7	95.0	49.0	45.0–53.0	50	10–90	47	36–58
V08290017a	288	45	327	16.6	93.4	48.0	44.5–52.0	95	60–125	67	41–94
V08303022b	288	51	313	16.7	96.9	56.5	53.5–59.0	60	30–85	83	41–126
V08503016a	298	49	306	16.5	92.8	44.5	44.0–45.0	45	25–70	83	51–114

Note: L_s, Lat., and Lon. coordinates have been rounded to save space.

spheric clouds – a detection rate of 0.24% (0.48% considering only images within 20° of the equator). There appears to be an association with the eastern Tharsis high altitude terrain and with Valles Marineris. With only a slight overabundance of the could-have-detected sequences in the 260–295 longitude range of the detections, these five detections represent a significant clustering. All of these detections fall within one of the longitude bands where Clancy et al. (2007) report detached hazes are prevalent. It is also intriguing that none of our equatorial mesospheric cloud detections fall in the L_s = 60–100° season where both Jaquin (1989) and Clancy et al. (2007) note an absence of high altitude hazes, and where no mesospheric clouds are detected by Mars Express instruments (Scholten et al., 2010; Määttänen et al., 2010).

The morphology of the equatorial mesospheric clouds is reminiscent of the Pathfinder "discrete linear clouds" discussed by Clancy and Sandor (1998) (see their Fig. 3), in that they are composed of "filaments" or "lineations". However, this is a highly subjective comparison, especially given the radically different viewing geometries of Pathfinder and THEMIS-VIS. Thus the THEMIS-VIS measurements cannot confirm the hypothesis that the particular clouds observed by Pathfinder were at mesospheric altitudes. They do however confirm the more general hypothesis that mesospheric aerosols form not just detached hazes but also discrete, highly structured clouds.

3.2.1. Comparison with GCM

Fig. 12 shows a comparison of the model winds and observed mesospheric cloud velocities for both the equatorial clouds and the mid-northern latitude clouds (further described in Section 3.3.2). While the agreement is generally good for the mid-northern latitude data, the agreement is not as good with the sparser equatorial data. The MarsWRF GCM generally predicts relatively light easterly winds at these altitudes and this season and time of day; similar values at these temporal and spatial locations are also predicted by other martian GCMs (Richardson et al., 2007). In contrast, seven out of the 10 equatorial measurements indicate the presence of a substantial easterly zonal wind.

If, as we will assume, the observed cloud motions accurately represent typical winds at these particular equatorial locations and these particular seasons and local times, there are several possible reasons that a GCM would predict different values. One possible cause is inaccuracies due to the model parameterization of gravity wave drag in the martian atmosphere at the altitudes under consideration here. As previously discussed, the lack of systematic direct wind measurements, at any altitude, makes it difficult to improve models in this direction. The measurements presented here will hopefully help with progress in this area. Another possible cause of the disagreement is the low spatial resolution of the GCM simulation (and GCMs in general). The equatorial wind measurements come from eastern Tharsis and western Valles Marineris, regions with dramatic changes in topography over relatively short distances. It is possible that a GCM may not be capturing high-resolution wind flows being generated by topography and/or eddies. A mesoscale simulation may provide some clarification of this issue, but is beyond the scope of this paper (as well as possibly being subject to the same issues discussed above and below). A final possible cause of the discrepancies is the large variation in equatorial wind speeds at these altitudes due to the influence of the solar thermal tide. Wind speeds can shift by as much as 100 m/s due to the passage of the Sun, and this would obviously have a very large impact on the quality of the comparison. GCMs are often "tuned" to try and capture the effect of tides as well as possible, but the "tuning" is done by validation against observations. Most observations exist in the lower middle atmosphere,

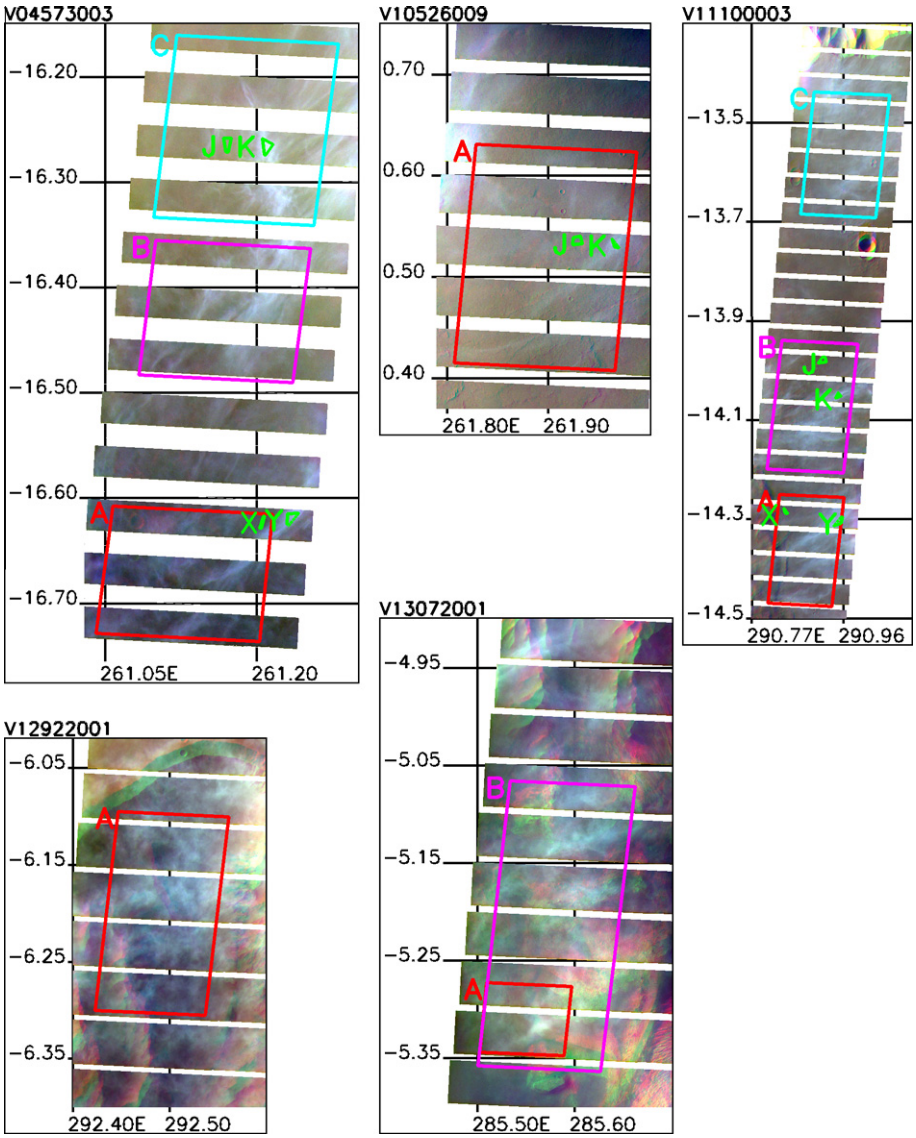

Fig. 7. Examples of equatorial mesospheric clouds, using enhanced color as defined in the text. Each image is map projected (the projection is sinusoidal) using the best-fit altitude and velocity. The grid lines give degrees east longitude and degrees north latitude. The large ROIs indicated by letters A–D are the correlation-ROIs, and their letters correspond to those in the first column of Tables 1–8. The smaller ROIs are cloud/cloud-free radiance pairs. Their labels correspond to the columns in Tables 9–11. Note that all of these images have been cropped to fit on the page while still showing the main cloud features. (For interpretation of the references to color in this figure legend, the reader is referred to the web version of this article.)

at a few local times, and are almost exclusively of temperature. Thus, by "tuning" to match one region (spatial and temporal) and (mainly) one variable, other regions and variables may become less well fit. The obvious solution is to try and fit a variety of regions and variables at the same time, but again, this has been limited to the extent that observations and data are available.

Note, however, that the recent comparison by Määttänen et al. (2010) of HRSC-measured mesospheric cloud speeds with a GCM that uniquely extends from the surface to the thermosphere – the LMD-MGCM (Forget et al., 1999) newly extended to the thermosphere by González-Galindo et al. (2009) – produced a good model-data agreement without any model tuning for mesospheric winds. The vertically-extended LMD-MGCM produced stronger easterly winds than the MarsWRF model used here, while the HRSC-measured and THEMIS-VIS-measured wind speeds are broadly similar. This suggests that extending the vertical domain of Mars GCMs is important for correctly capturing winds in the equatorial mesosphere, but further investigation is needed before any firm conclusions can be drawn about the reasons for the differences in the two models.

3.3. Mid-latitude mesospheric clouds

All of the mid-latitude mesospheric clouds were discovered serendipitously in images targeted as part of a "Frontal Storm Survey" (Inada et al., 2007) which had the intended goal of capturing high-resolution views of the major storm systems that are occasionally observed by MOC-WA (Wang and Ingersoll, 2002; Wang et al., 2005) in northern mid-latitudes in the fall and winter. THEMIS-VIS did not succeed in capturing any usable images of the intended storm systems, due in part perhaps to the late afternoon solar time of the THEMIS-VIS observations. (THEMIS has to date been constrained to a nadir-pointing configuration, and the ODY orbit is Sun-synchronous with a local solar time allowed to drift between 4 and 5:30 pm.) This late local time meant that all THEMIS-VIS images acquired of the two targeted storm track regions in Acidalia

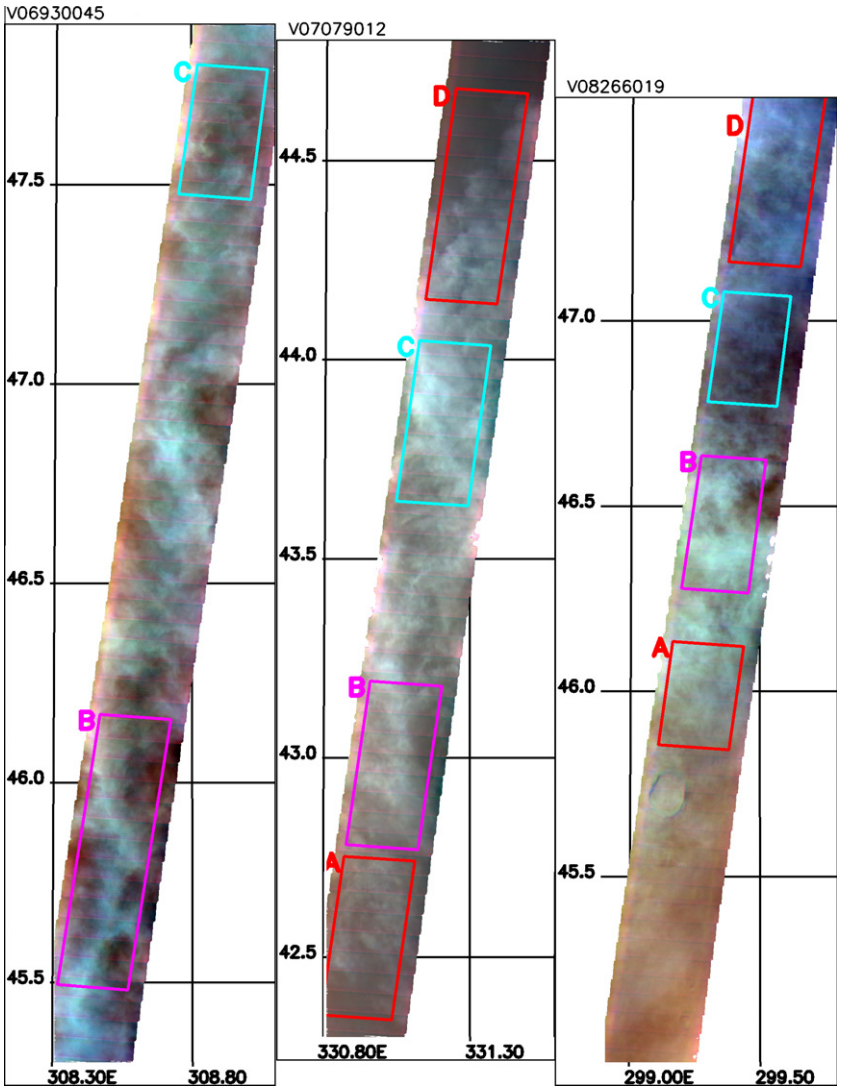

Fig. 8. Examples of the "clumpy" class of mid-latitude mesospheric clouds. For V06930045 and V07079012 we have filled in narrow gaps between framelets by extrapolating from neighboring pixels. Otherwise the same as Fig. 7. Note that all of these images have been cropped to fit on the page while still showing the main cloud features.

and Amazonis Planitiae between $L_s = 200°$ and $L_s = 300°$ were of surfaces with incidence angles greater than 90°. All of the mesospheric clouds were detected in this L_s range. Once the typical incidence angles fell below 90°, no further mesospheric clouds were detected. All of the detected mid-latitude mesospheric clouds had 92–100° incidence, and none of the observations past $L_s = 300°$ had incidence angles in this range. Thus, the >90° incidence angles may have been crucial to the detection of the mesospheric cloud features, but this is impossible to prove because of the correlation between seasons and incidence angle.

The distribution of mesospheric detections, as compared with all $L_s = 200–300°$ northern mid-latitude frontal storm survey image sequences having both blue and green filters, is shown in Fig. 13. Each mid-latitude subclass is plotted with a different symbol. The distribution of mesospheric detections appears similar to the distribution of all sequences in the Acidalia region, with detections in 17%, 29 of 174 sequences. Only one out of 36 Amazonis sequences yielded a detection. This weakly suggest that either some intrinsic feature of the Acidalia region leads to more high altitude clouds, or that the slight difference in the latitude of the two survey regions has an impact on the presence or detectability of high-altitude clouds.

Fig. 14 shows several trends in the altitude of the mid-latitude mesospheric clouds. All of the clouds above 60 km altitude are found in $L_s = 200–240°$, have incidence angles greater than 96°, and are in the "clumpy" morphology subclass. Thus, it appears that later season, low-incidence, and linear or linear-periodic clouds are confined to lower mesospheric altitudes. However, since approximately three times as many incidence >96° detections occur in $L_s = 200–240°$ as in $L_s = 240–300°$, it is not clear whether the trends are related to the seasonal prevalence of certain types of clouds, or to their detectability as a function of incidence angle.

The incidence angles we report are for the planet's surface at the location of the mesospheric cloud correlation-ROIs, and of course high altitude clouds are still directly illuminated for surface incidence angles in the 90–100° range. Since we still see surface features at incidence angles greater than 95°, multiple scattering is obviously very important, and so we cannot make simple assumptions about what altitude a feature must have to be detected. However, directly illuminated cloud features have a detectability advantage over lower altitude clouds, and given the observed correlations between incidence angle and cloud altitude, and the fact that we have not positively identified any low altitude clouds with incidence >92°, our preferred hypothesis is that cloud

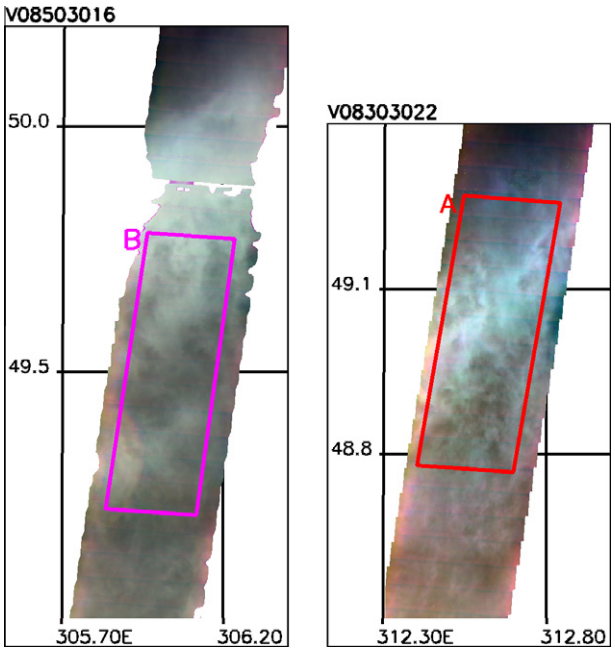

Fig. 9. Examples of the "linear" class of mid-latitude mesospheric clouds. In V08503016, there are some gaps in the image caused by saturated pixels in the green filter image. We have extrapolated to fill the narrower gaps. Otherwise the same as Fig. 7. Note that each of these images have been cropped to show only a small portion of the full image, since in both cases the remainder of the image lacks prominent cloud features. (For interpretation of the references to color in this figure legend, the reader is referred to the web version of this article.)

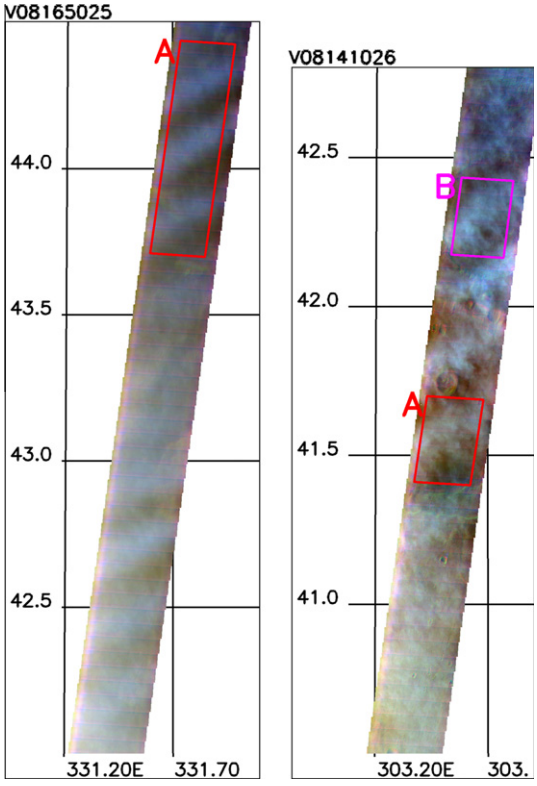

Fig. 10. Examples of the "linear-periodic" class of mid-latitude mesospheric clouds. Otherwise the same as Fig. 7. Note that all of these images have been cropped to fit on the page while still showing the main cloud features.

aerosols are present at a range of altitudes during much of the northern fall-winter period, and the altitude of the aerosols that

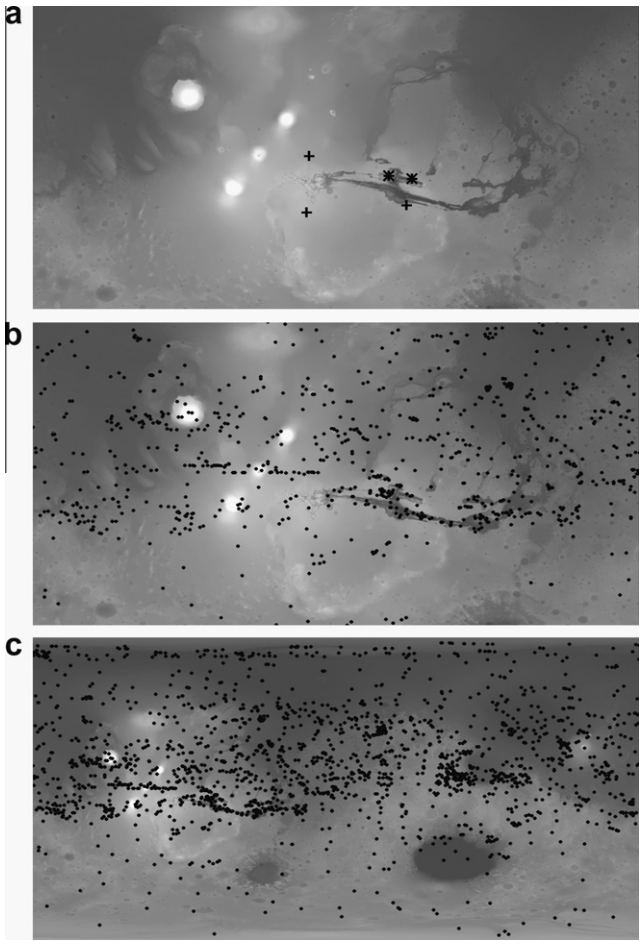

Fig. 11. (a) Map of the locations where we have observed equatorial mesospheric clouds. Clouds in the "filamentary" subclass are marked with a +, and non-filamentary clouds are marked with an asterisk. In cases where there are multiple mesospheric cloud ROIs in a single THEMIS-VIS image sequence, we have plotted only one from each subclass. (b and c) Location of all of the THEMIS-VIS images that could have detected mesospheric clouds. (c) The entire planet. (b) The same region of the planet as in (a). The background for each map is grayscale-coded topography as measured by the Mars Orbiter Laser Altimeter.

dominate the spatial contrast is selected by the geometry of the observation. Thus, when the incidence angle is low, the more diffuse high-altitude features are overwhelmed by the lower altitude cloud, but at higher incidence angle the lower altitude aerosols contribute much less to the radiance reaching THEMIS-VIS, and so the higher altitude features become visible.

3.3.1. Comparison with daily global maps

In daily global maps (DGMs) of Mars assembled by Wang and Ingersoll (2002) from MOC-WA images, clouds are ubiquitous over northern mid-latitudes in the L_s = 240–300° period. We have therefore compared our images of mesospheric clouds with the DGMs in an attempt to place them in context with the global cloud field. Although the "polar streak" clouds and polar lee waves described by Wang and Ingersoll (2002) are certainly prevalent in the general vicinity of the mesospheric cloud images, in almost all cases we cannot match any of the features in the DGMs with features in the THEMIS-VIS images acquired on the same day. Since the wind speeds in this winter mid-latitude region of the mesosphere are high and the MOC-WA images are not concurrent with the THEMIS-VIS images, since THEMIS-VIS and MOC-WA observe at difference local times, and since the THEMIS-VIS field of view is very narrow compared to the MOC DGMs, it is not at all surprising that

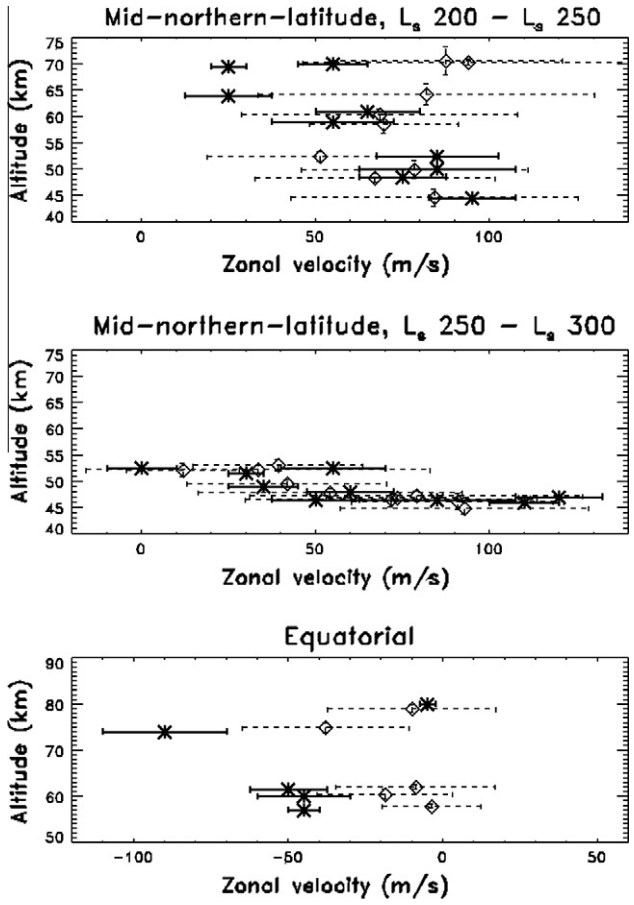

Fig. 12. Comparison of THEMIS-VIS zonal velocity measurements with GCM values. Asterisks and solid lines show THEMIS-VIS measurements, diamonds and dashed lines show GCM values. The error bars correspond to our reported confidence intervals for the measurements, and to $\pm 2\sigma$ for the GCM values (the standard error σ of the GCM values is defined in the text). We have suppressed the altitude error bars for the measurements, because they are quite small (±2 km typically) on this scale. For any given THEMIS-VIS image sequence, we show only one measurement and its corresponding GCM value. We chose the measurement with the narrowest confidence interval.

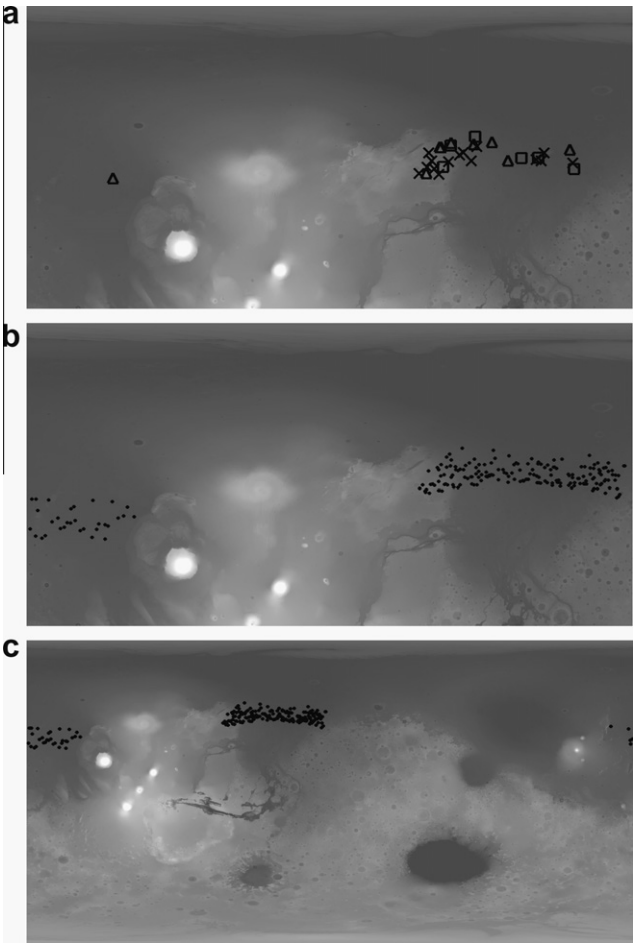

Fig. 13. (a) Map of the locations where we have observed mid-latitude mesospheric clouds. Clouds in the "clumpy" subclass are marked with an "X", clouds in the "linear" subclass with a triangle, and clouds in the "linear-periodic" subclass with a square. In case where there are multiple mesospheric cloud ROIs in a single THEMIS-VIS image sequence, we have plotted only one from each subclass. (b and c) Location of all of the mid-latitude THEMIS-VIS images in the L_s = 200–300° period that could have detected mesospheric clouds. (c) The entire planet. (b) The same region of the planet as in (a). The background for each map is grayscale-coded topography as measured by the Mars Orbiter Laser Altimeter.

feature matching between the two instruments is difficult. It is also of course possible that some types of mesospheric clouds have no connection at all with the cloud field normally observed by MOC.

We have, however, identified two examples where an overlay of the THEMIS-VIS mesospheric image onto the MOC DGM seems to show a pattern similar to nearby MOC cloud features. These two examples are shown in Figs. 15,16. We do not expect an exact match because the two images are not concurrent, and so the feature match represents a subjective judgement. Accepting for the sake of argument that the match is real, we have a possible identification of the linear mesospheric features with the "polar streak" clouds that are the dominant feature of the polar hood as described by Wang and Ingersoll (2002). This implies that some of the familiar polar hood cloud extends up to 55 km in altitude, or that polar streak clouds and linear mesospheric clouds are connected by some dynamical process.

3.3.2. Comparison with GCM

Both Tables 6–8 and Fig. 12 compare our velocity measurements with WRF GCM results generated as previously described. Unlike the equatorial case, our mid-latitude velocities are consistent with the GCM model predictions. Both the data and model output show a generally westerly (eastward) wind of order tens, up to a hundred, m/s, and a trend towards lower velocities at higher altitudes.

The exception to the generally good agreement between observations and model predictions occurs at altitudes of 65 km and above. Here, the GCM model predicts westerly winds that are stronger than the observations. This may be due to the use in the GCM of the prescribed dust opacity function based on MGS year 1 observations (identical to the Mars Climate Database "MGS scenario" for dust described by Lewis et al. (1999)). The GCM predictions that differ the most from the wind measurements all occur near L_s 225°, a season in which major regional dust storms are the norm. Thus the observed (by MGS-TES, *e.g.*, Smith, 2004) differences in the timing and location of the regional storms between MGS year 1 and the year of our THEMIS-VIS measurements (MGS year 3) could account for differences between the model and the measurements during this period.

Both the model and our measurements also show wide variability in the zonal wind at all levels, even to the point of occasional transient easterlies. This is consistent with the expected intense wave activity in the fall – winter mid-latitudes. It also demonstrates that this eddy activity extends into the mesosphere where it might be important for the processes that form the observed clouds and cloud features.

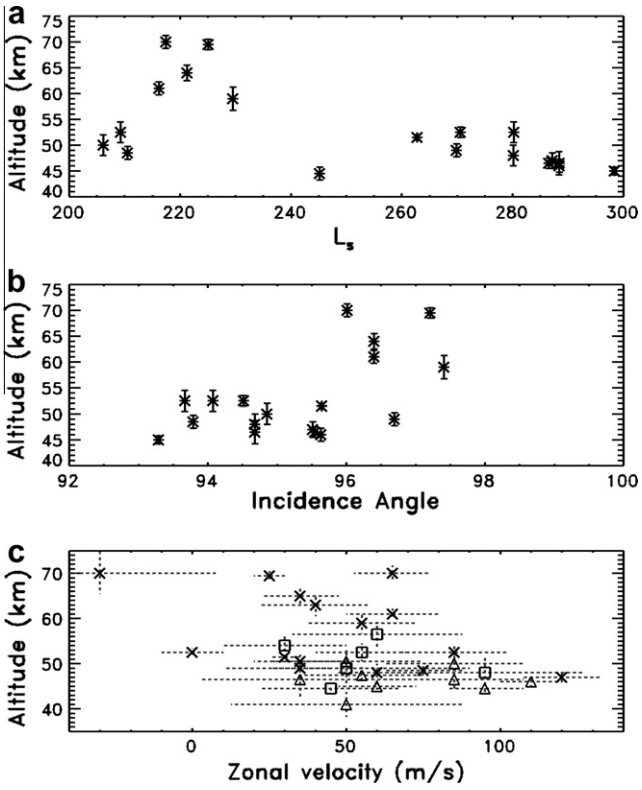

Fig. 14. Altitude as a function of (a) season and (b) incidence angle for mid-latitude mesospheric clouds. (c) Altitude and velocity for the various subclasses of mid-latitude mesospheric clouds. Clouds in the "clumpy" subclass are marked with an "X", clouds in the "linear" subclass with a square, and clouds in the "linear-periodic" subclass with a triangle. For any given THEMIS-VIS sequence, we show only one measurement from each subclass. We chose the measurement with the narrowest confidence interval.

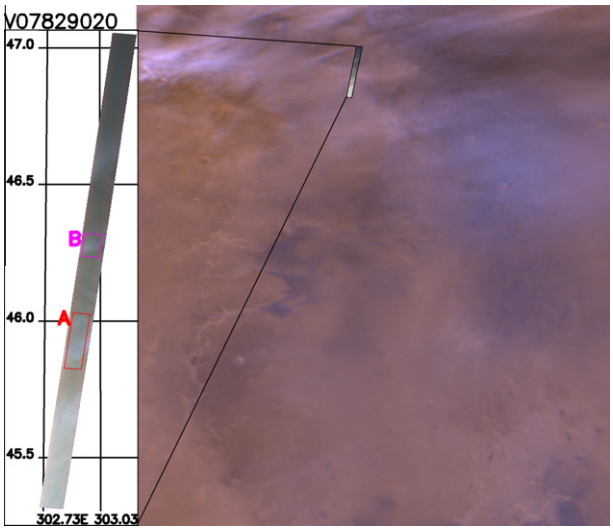

Fig. 15. Comparison of a THEMIS-VIS high-altitude cloud image with a portion of a MOC-WA DGM from the same day. The projection and labeling of the THEMIS-VIS image are the same as in Fig. 7.

4. Radiative transfer model

In order to compare our cloud measurements with previous work, and to provide insight into their physical significance, we apply a simple radiative transfer model to a subset of our data. We have chosen the standard, public domain, plane parallel discrete ordinates model DISORT (Stamnes et al., 1988). Prior uses of DISORT for martian clouds include Wolff et al. (1999) and Benson et al. (2003). The choice of a plane parallel model immediately limits us to considering only the equatorial clouds, which are observed at incidence angles significantly less than 90°. Investigation of the properties of the mid-latitude twilight clouds will have to wait for a more sophisticated three-dimensional modeling approach, which is beyond the scope of this work.

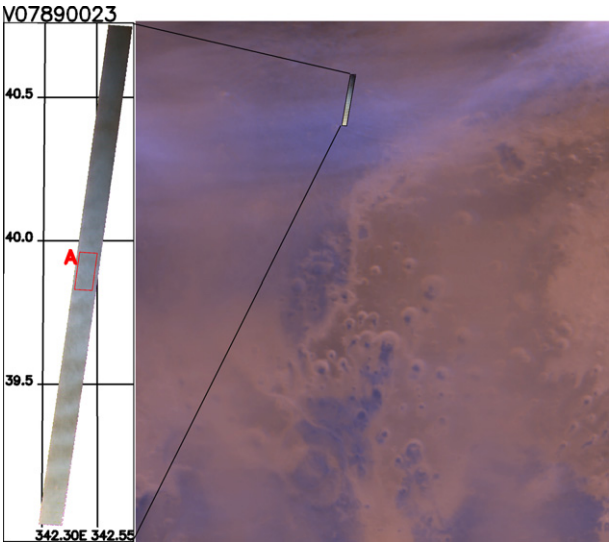

Fig. 16. Comparison of a THEMIS-VIS high-altitude cloud image with a portion of a MOC-WA DGM from the same day. The projection and labeling of the THEMIS-VIS image are the same as in Fig. 7.

We apply our DISORT model to portions of three equatorial mesospheric cloud images. We begin by drawing a pair of regions of interest on the image; one region with minimal blue filter brightness and thus apparently minimal cloud opacity; and one region with maximal blue filter brightness and thus maximal cloud. These regions are shown in Fig. 7. For V04573003 and V11100003, we have selected two such pairs, in order to check the consistency of our model results in different portions of the image. V10526009 has only a small area of mesospheric cloud, and so we have defined only one region of interest pair. For each filter, we take the mean radiance in the selected regions, labeling them the "cloud radiance" and the "cloud-free radiance". The radiance calibration standard errors (McConnochie et al., 2006), are much larger than the standard deviations of the radiance in our selected regions, and so we adopt them as the measurement standard errors for purposes of our calculations here.

The models include a Lambertian surface as the lower boundary, Rayleigh scattering by gaseous atmospheric constituents, a lower-atmosphere aerosol component with properties consistent with previous work, and a mesospheric aerosol component. Our DISORT models use 64 streams and 8 vertical layers, each 10 km thick, with the bottom of the lowest layer being at the surface and the top of the top layer at 80 km. For each layer we specify that layer's optical depth, single-scattering albedo (SSA), and phase function. The optical depth of a layer is a sum of the optical depths of whichever of the three components (Rayleigh scatterers, lower-atmosphere aerosols, and/or mesospheric aerosols) are present in the layer. The SSA and phase functions are weighted averages of the component values, where the weights are the component optical depths in that layer. The rayleigh scattering is determined by a density profile that we derive via the hydrostatic equation from a typical low latitude MGS-TES temperature profile (*e.g.*, Conrath et al., 2000). We adjust the surface pressure to account for the altitude of the local surface in each model.

4.1. Lower atmosphere and surface

MGS-TES (*e.g.*, Smith et al., 2001) measurements show very low dust optical depths at the time and place of all of the observations we model, and so the lower aerosol component is assumed to contain only water ice aerosols that are defined to be consistent with Clancy et al. (2003) "type 1" water ice aerosols. Thus, we use the Clancy et al. (2003) measured phase function; adopt a particle size distribution with 1.5 μm effective radius (r_{eff}) and an effective variance (v_{eff}) of 0.1 for purposes of scaling the opacity as a function of wavelength; and assume zero water ice aerosol below 20 km altitude. Above 20 km, we assume that the water ice aerosol opacity in any given layer scales with the gas density, up to an arbitrary upper boundary of 60 km. We have found that the choice of this upper boundary has no effect on our results. (Note that these lower-atmosphere water ice aerosols are not readily apparent in the THEMIS-VIS images simply because they have little spatial variability at the THEMIS-VIS scale.)

The normal albedo of the surface and the optical depth of the lower aerosol layer are constrained using our cloud-free radiance measurement and "nearby" MGS-TES aerosol optical depth measurements. We presume that, since the mesospheric aerosols are invisible to THEMIS-IR, they are also invisible to MGS-TES. For the case of V10526009, we defined "nearby" as within 3 sols of time, 5° of longitude and 0.5° of latitude, and adopted the mean of TES aerosol retrievals in this region. For V11100003, we instead used 1 sol and 1.5° of latitude as the limits. THEMIS-IR aerosol retrievals (Smith et al., 2003) are available concurrent with V11100003, and these measurements are consistent, within the uncertainties reported by Smith et al. (2003), with our adopted MGS-TES values. In the vicinity of V04573003, no TES or THEMIS-IR aerosol retrievals are available, due to low surface temperatures.

Since the TES retrievals consider only absorption, they need to be adjusted to provide an estimate of the full extinction optical depth. According to Smith (2004), the appropriate adjustment is to multiply the TES optical depth by 1.5. We also of course must adjust the TES optical depth to compensate for the difference in extinction cross-section between the wavelength where it is defined (12.1 μm), and the wavelengths of the THEMIS-VIS filters. We calculate the cross-sections as a function of wavelength using standard Mie theory (*e.g.*, Bohren and Huffman, 1983) as implemented in the publicly available code, DMiLay (ftp://climate.gsfc.nasa.gov/pub/wiscombe/Single_Scatt/Coated_Sphere). The water ice indices of refraction (real and imaginary) are from Warren (1984).

Where the TES retrievals are available, we use the TES derived optical depth together with the above described assumptions about the aerosol properties, and iteratively adjust the surface albedo until the DISORT model matches the cloud-free radiance. We perform this procedure independently for each THEMIS-VIS filter, and, for simplicity and efficiency, we model only the single discrete wavelength at the center of the bandpass for each filter. Since the assumption that the surface is a Lambertian scatterer is probably a poor one, we do not expect to obtain a normal albedo that is consistent with previous work or even representative of the real normal albedo of the surface. Rather, we obtain an effective albedo that happens to be appropriate for the high incidence angle geometry of the THEMIS-VIS measurements. Estimates of the true photometric properties of the surface at high incidence angle are not available, and so solving for an effective albedo represents a best guess. More importantly, the function of the albedo in our model is merely to allow the surface/lower atmosphere components of our model to match the observed cloud-free radiance. Since we always achieve such a match, the primary effect of trading off albedo for lower-atmosphere optical depth is to alter the angular distribution of radiation reaching the mesospheric region from below. This angular distribution has only a secondary effect on our model. We have experimented with decreasing the lower-atmosphere opacity by a factor of two, which leads to unrealistically high surface albedos, but has negligible impact on our derived mesospheric optical depths and the perturbation to our derived particles sizes is small compared with other sources of uncertainty.

Since V04573003 lacks TES or THEMIS-IR measured optical depths, we follow a slightly more complicated procedure for that case. We start with the blue filter normal albedo derived for V10526009, then iterate the blue filter optical depth to match the blue cloud-free radiance. Since the blue filter albedo of the martian surface is very low, its influence on the observed radiance is small when the optical depth is high, as it is for V04573003. Having derived the blue filter optical depth, we simply scale it to the other filters using the Mie-derived cross-sections, and then iterate for the albedo in these filters as previously described.

For each pair of radiance measurements, we crucially assume that both the surface albedo and the lower-atmosphere aerosol component are the same in the (mesospheric) cloud-free region and the mesospheric cloud region. The mesospheric clouds in V12922001 and V13072001 are in regions of prominent surface features, which is why we have not attempted to apply our model to them. For the image sequences that we do model, the cloud and cloud-free regions are drawn to minimize the possibility of such surface variations, and it is clear from Fig. 7 that the mesospheric aerosols are the dominant source of contrast in their vicinity. Since Fig. 7 is projected at the measured aerosol altitude, significant surface contrasts lead to obvious color mis-alignments, as would low-altitude aerosol variations if they were present.

The other crucial assumption that we make about the relationship between the cloud-free radiance and the cloud radiance is that the cloud-free region actually contains zero mesospheric aerosol, rather than simply less mesospheric aerosol than the cloud features themselves. We have no way to verify this assumption, but it is necessary, because without it we have no way to constrain the effective surface albedo. If there is a mesospheric aerosol contribution to the radiance that we have labeled cloud-free, it would mean that we have overstated the lower atmosphere/surface contribution to the observed radiance in the cloudy areas, and understated the mesospheric contribution to the radiance in these areas. Since we are working in a regime with a positive relationship between optical depth and observed radiance, any mesospheric aerosol contamination of the "cloud-free" areas leads us to underestimate the mesospheric aerosol optical depth.

4.2. Mesospheric aerosols

Having used the above assumptions to establish the contributions of the surface and lower atmosphere, we explore a range of possibilities for properties of the mesospheric clouds. We must first specify the upper and lower altitude boundaries of the mesospheric clouds (we choose 70–80 km), but we have found these boundaries have no effect on the modeled radiances, and so they are extraneous to the modeling problem. The factors that do influence the radiance we observe, as modeled by DISORT, are the vertical extinction optical depth, the single-scattering albedo (SSA), and the single-scattering phase function of the aerosols, all of which themselves are functions of wavelength. Since this modeling problem is highly under-determined, we first simplify by adopting a Henyey–Greenstein phase function (Henyey and Greenstein, 1941) for the mesospheric aerosols, which can be described by a single parameter, g (the asymmetry parameter), at each wavelength. Next, we impose a physical description of the aerosol particles, which gives us, via Mie theory, g_λ, SSA_λ, and the mean particle extinction cross-section $\langle\sigma\rangle_\lambda$, at the wavelengths λ of all of the THEMIS-VIS filters. Now, the problem is overdetermined for any given physical description – specifying the optical depth

in any one filter yields the optical depth in the rest, via their relative values of $\langle\sigma\rangle_\lambda$, and so a single optical depth yields radiance in all three or four filters. We arbitrarily choose the blue filter as the wavelength at which to specify optical depth. Treating the observed cloud radiances as random variables with standard errors equal to the THEMIS-VIS calibration standard errors, we have a χ^2, and so we find the blue filter optical depth by iteratively adjusting it until the χ^2 is minimized. The probability of observing a χ^2 as large as the minimized χ^2 can be interpreted as a likelihood for the best fit with a particular physical description of the aerosols. Thus, we can reject any physical description that yields a best fit likelihood lower than some arbitrary cutoff.

The aerosols that we have chosen to consider for the mesospheric clouds are:

1. CO_2 ice (indices of refraction from Hansen (1997)).
2. Water ice (indices of refraction from Warren (1984)).
3. Dust (indices of refraction from Wolff et al. (2006)).
4. Dust core with CO_2 ice shell: core radii 20%, 40%, 60%, and 80% of the total particle radius.
5. Dust core with water ice shell: core radii 20%, 40%, 60%, and 80% of the total particle radius.

For each aerosol type, we consider particle sizes ranging from $r_{\text{eff}} = 0.05$ μm to $r_{\text{eff}} = 5$ μm. We have chosen these limits because in most cases they appear to bound the region where significant model likelihood is observed. We test particle size with sampling intervals of 0.01 μm between 0.05 and 0.2, 0.1 between 0.2 and 2.0, and 0.5 from 2.0 to 5.0. For all cases, we use a simple shape for the mesospheric particle size distribution: a gamma distribution with v_{eff} of 0.2, consistent with Chassefière et al. (1992). An experiment with $v_{\text{eff}} = 0.1$ showed negligible changes in our results.

The radiances, geometric parameters, and assumed surface and lower-atmosphere properties used for our models are shown in Table 9. All models of a given ROI pair use the same assumptions for the surface and lower atmosphere. We construct separate models with optimized optical depth for each particle composition and particle size. In the results tables (Tables 10 and 11) we show the particle size, optical depth, and, where applicable, the core radius for the model with the highest likelihood. We also show confidence intervals for these parameters that include all models with likelihood greater than our chosen threshold of 1%. Particle compositions that yield no model likelihoods greater than this threshold are indicated with a '–' in the table.

For V04573003 and V11100003, we have included in the results tables only the ROI pair with the highest model likelihood from each image sequence. In both of the sequences with two ROI pairs, both ROI pairs yielded similar likelihood maxima with similar particle properties. The confidence intervals are listed as "any" for V10526009 because for this image sequence all the models yielded likelihoods greater than the cutoff. The lack of precision with this image is a result of its short exposure time, which leads to high uncertainty in the radiance calibration, and of the low contrast of its aerosol features.

Note that when the particle size confidence interval is listed as "any", the τ confidence interval simply reflects the range of values observed in the searched parameter space, and so is not a true constraint on the optical depth. Also note that once the optical depth is larger than ~5, changing it has very little effect on the modeled radiance, and so optical depth limit values greater than 5 are numerical artifacts and can be interpreted simply as "very large".

For the best fit particle size, optical depth, and core radius, we present various other quantities intended both as reality checks and as indicators of the physical significance of the results. In order to calculate number density we have assumed a physical depth for the clouds of 10 km. This 10 km value should be considered to be merely an approximate upper limit on the vertical extent – given their 100 m scale horizontal structure and the 2 km precision with which their altitude is constrained, a vertical extent larger than 10 km seems unlikely. (Note also that Montmessin et al. (2007) were in one instance able to place an upper limit of 10 km vertical extent for the thickest part of an equatorial mesospheric cloud based on its shadow.)

Table 9
Radiative transfer ROIs: mean properties of each cloud/cloud-free pair.

Property	ROI pair				
	V04573003		V10526009	V11100003	
	J, K	X, Y	J, K	J, K	X, Y
Cloud-free ROI viewing geometry					
E. Lon.	261.172	261.207	261.929	290.91	290.842
N. Lat.	−16.264	−16.623	0.536	−13.98	−14.283
Inc. (°)	80.02	80.24	68.96	77.89	77.96
Cloud ROI viewing geometry					
E. Lon.	261.209	261.235	261.966	290.95	290.95
N. Lat.	−16.266	−16.619	0.522	−14.05	−14.306
Inc. (°)	80.06	80.26	69.00	77.95	78.06
Cloud-free radiance $((I/F) \times 10^{-2})$					
At 0.425 μm	2.86	2.67	3.73	2.00	2.16
At 0.540 μm	5.11	4.61	7.30	3.34	3.39
At 0.654 μm	8.27	7.49	14.8	–	–
At 0.749 μm	9.90	8.97	18.4	6.03	5.96
Cloud radiance $((I/F) \times 10^{-2})$					
At 0.425 μm	3.40	3.19	4.93	2.95	3.22
At 0.540 μm	5.59	5.15	7.75	4.29	4.47
At 0.654 μm	8.72	8.15	15.1	–	–
At 0.749 μm	10.4	9.71	18.6	7.18	7.45
Lower-atmosphere aerosol component optical depth, τ_{low}					
At 0.425 μm	0.54	0.49	0.44	0.23	0.23
At 12.1 μm	0.28	0.25	0.23	0.12	0.12
Effective surface albedo, A_{eff}					
At 0.425 μm	0.023	0.023	0.020	0.023	0.034
At 0.540 μm	0.271	0.237	0.16	0.12	0.12
At 0.654 μm	0.579	0.522	0.43	–	–
At 0.749 μm	0.727	0.661	0.55	0.29	0.284

For the mass fraction of CO_2, we must chose a portion of the atmospheric column to which to compare the column mass of condensate; we have chosen a 10 km vertical column immediately below the measured cloud altitude, determining its mass from the same MGS-TES-derived density profile used to calculate Rayleigh scattering. For the relative mass of H_2O, we compare the mass of H_2O in the aerosols with the maximum mass of H_2O vapor (*i.e.*, mass at saturation) that could be contained in a 10 km vertical column at a reasonable upper bound (see Clancy and Sandor, 1998) temperature for the mesosphere of 160 K. With τ_{dust} we suppose that the refractory cores of the heterogeneous aerosols must have been present before the condensate shells formed, and calculate the optical depth that they would have had before the condensation occurred.

4.3. Constraints imposed by THEMIS-IR and MGS-TES

Both V04573003 and V11100003 were accompanied by simultaneously acquired THEMIS-IR images. Neither IR image shows any evidence for cloud features, which provides a powerful constraint on the aerosol composition. Also, if we suppose that the dust cores of the heterogeneous aerosols must be present over a somewhat wider region than the locus of condensation itself, the very low dust optical depths measured by MGS-TES also provide a constraint. Since THEMIS-IR and MGS-TES routinely measure dust and water ice optical depth using absorption bands centered at 9.3 and 12.1 μm, respectively, (Smith et al., 2001, 2004) we calculate optical depths at these wavelengths to see if either instrument would have detected the aerosol in question.

Table 10
Radiative transfer model results: homogeneous mesospheric cloud aerosols-preferred models (see text) in boldface.

ROI pair	V04573003b J, K	V10526009 J, K	V11100003 J, K	V11100003 749 nm excluded J, K
CO_2 ice				
r_{eff} (μm)	**0.10 [0.08–0.11]**	**0.05 [any]**	–	**1.5 [0.8–1.8]**
τ at 0.425 μm	**0.22 [0.14–0.27]**	**0.074 [0.074–0.31]**	–	**0.50 [0.38–0.57]**
τ at 9.3 μm	**0.00**	**0.00**	–	**0.05**
τ at 12.1 μm	**0.00001**	**0.00001**	–	**0.02**
n[a] (cm^{-3})	**2080**	**19,400**	–	**6.42**
Mass fraction[b]	**0.07%**	**0.08%**	–	**0.07%**
Precipitable[c] (μm)	**0.04**	**0.05**	–	**0.44**
H_2O ice				
r_{eff} (μm)	0.10 [0.08–0.12]	0.05 [any]	–	–
τ at 0.425 μm	0.22 [0.13–0.38]	0.073 [0.073–0.44]	–	–
τ at 9.3 μm	0.004	0.005	–	–
τ at 12.1 μm	0.03	0.03	–	–
n (cm^{-3})[1]	3710	34,700	–	–
Relative mass[d]	6.5	7.6	–	–
Precipitable (μm^3)	0.07	0.09	–	–
Dust				
r_{eff} (μm)	0.08 [0.07–0.09]	0.10 [0.05–0.4]	0.5 [0.5–0.5]	0.4 [0.4–0.5]
τ at 0.425 μm	0.30 [0.23–0.40]	0.20 [0.13–0.94]	1.6 [1.6–1.6]	1.0 [1.0–1.6]
τ at 9.3 μm	0.04	0.02	0.30	0.14
τ at 12.1 μm	0.004	0.002	0.03	0.013
n (cm^{-3})[1]	5350	1380	153	141

[a] Number density, assuming that the physical depth of the cloud is 10 km.
[b] Mass of CO_2 condensate as a fraction of the mass of the atmosphere between 70 and 80 km (for V04573003 and V10526009), or between 50 and 60 km (for V11100003).
[c] Depth of condensate if spread uniformly in solid phase on a horizontal surface.
[d] Ratio of the mass of H_2O condensate to the mass of H_2O vapor in a 10 km, saturated column, at 160 K.

Table 11
Radiative transfer model results: heterogeneous mesospheric cloud aerosols-preferred models (see text) in boldface.

ROI pair	V04573003b J, K	V10526009 J, K	V11100003 J, K	V11100003 749 nm excluded J, K
Dust core, CO_2 ice shell				
r_{eff} (μm)	**0.09 [0.08–0.11]**	**0.05 [any]**	1.4 [0.7–4.0]	**0.7 [0.5–4.0]**
Core radius fraction	**0.8 [0.2–0.8]**	**0.2 [any]**	0.6 [0.4–0.8]	**0.8 [0.2–0.8]**
τ at 0.425 μm	**0.25 [0.14–0.41]**	**0.075 [0.075–23]**	1.3 [0.75–2.8]	**1.1 [0.38–23]**
τ at 9.3 μm	**0.016**	**0.0003**	0.30	**0.17**
τ at 12.1 μm	**0.0015**	**0.00004**	0.08	**0.02**
τ_{dust} at 9.3 μm[a]	**0.014**	**0.0003**	0.15	**0.15**
n (cm^{-3})[b]	**3040**	**19,600**	18.4	**55.5**
Mass fraction[c]	**0.04%**	**0.08%**	0.1%	**0.03%**
Precipitable[d] (μm)	**0.02**	**0.08**	0.8	**0.2**
Dust core, H_2O ice shell				
r_{eff} (μm)	0.10 [0.08–0.12]	0.05 [any]	0.8 [0.8–3.5]	0.7 [0.6–4.5]
Core radius fraction	0.6 [0.2–0.8]	0.2 [any]	0.8 [0.4–0.8]	0.8 [0.4–0.8]
τ at 0.425 μm	0.25 [0.13–0.44]	0.073 [0.073 –1.8]	1.6 [1.4–2.7]	0.97 [0.79–63]
τ at 9.3 μm	0.013	0.005	0.32	0.17
τ at 12.1 μm	0.019	0.03	0.17	0.09
τ_{dust} at 9.3 μm[1]	0.009	0.0003	0.25	0.14
n (cm^{-3})[2]	3080	34,100	59.3	53.1
Relative mass[e]	4.2	7.4	26	15
Precipitable (μm)[4]	0.05	0.09	0.3	0.2

[a] The vertical optical depth that the dust cores would have if not coated by condensate.
[b] Number density, assuming that the physical depth of the cloud is 10 km.
[c] Mass of CO_2 condensate coatings as a fraction of the mass of the atmosphere between 70 and 80 km (for V04573003 and V10526009), or between 50 and 60 km (for V11100003).
[d] Depth of condensate if spread uniformly in solid phase on a horizontal surface.
[e] Ratio of the mass of the H_2O condensate coatings to the mass of H_2O vapor in a 10 km, saturated column, at 160 K.

Our models for V04573003 and V10526009 (considering the best fit) yielded particle sizes and optical depths small enough to be invisible to the infrared instruments. However, both THEMIS-IR and MGS-TES arguments rule out the dust and the heterogeneous aerosols for V11100003. THEMIS-IR measures dust optical depth with an uncertainty of about 0.04 (Smith, 2004), and all of these cases in V11100003 yield 9.3 μm optical depths greater than 0.17 for the best fit (and greater than 0.12 considering the full range of the confidence intervals). Smith et al. (2001) give 0.05 as the uncertainty for MGS-TES optical depths, and the mean MGS-TES dust optical depth in the vicinity of V11100003 was 0.03, so the $\tau = 0.14$ of dust optical depth required as condensation nuclei for the aerosols in our model are unlikely to be present, even if we supposed that all of the dust aerosol was (improbably) in the mesosphere.

Note that, for the first V11100003 column in the results tables, there are no solutions that meet our likelihood threshold for homogeneous condensate aerosols. Thus, now that we have used THE-

MIS-IR and MGS-TES constraints to rule out dust and heterogeneous aerosols for this image, we are left with no viable solutions. In words, neither heterogeneous nor homogeneous aerosols with any of the compositions that we have considered yields an acceptable match to the available data when all three V11100003 channels are considered.

4.4. Models with the 749 nm filter excluded

This problem motivates us to consider models that ignore the 749 nm filter radiances. These models are shown in the final column of Tables 10 and 11. Since the martian surface albedo is highest in the 749 nm filter, its influence on the models is also greatest in the 749 nm filter. Thus the assumption of constant surface albedo between the cloud and cloud-free radiance ROIs is most critical at this wavelength. Although we strove to minimize the chance of albedo contrasts, V11100003 has more prominent surface features than the other images, and so albedo variations are a plausible explanation for lack of tenable results when the 749 nm filter is included.

With the 749 nm filter excluded, we find that there are both homogeneous and heterogeneous solutions that meet our likelihood threshold. However, homogeneous water ice is still fails to meet the likelihood threshold, and the THEMIS-IR and MGS-TES constraints still rule out dust and heterogeneous water ice. The THEMIS-IR and MGS-TES constraints would also appear at first glance to rule out the heterogeneous CO_2 ice solutions, since the 9.3 μm optical depth of the best fit is 0.17. However, unlike the 749-nm-filter-included case, when we consider the full range of the confidence intervals some of the allowed CO_2 ice solutions have 9.3 μm optical depths less than THEMIS-IR measurement uncertainty of 0.04. Specifically, the CO_2 ice solutions below this threshold were those with 40% core radius fraction and $r_{\text{eff}} \leqslant 1.1$ and those with 0% or 20% core radius fraction and $r_{\text{eff}} \leqslant 1.2$. The bottom line is that *both* heterogeneous and homogeneous CO_2 ice models yield viable solutions when the 749 nm filter is excluded.

For the sake of consistency, we have experimented with neglecting the 749 nm filter in the V04573003 cases and found no change in the best fits or the confidence intervals. In fact, neglecting *both* the 654 nm filter and the 749 nm filters also yields no change in the V04573003 best fits, and causes only a slight widening of the confidence intervals.

4.5. Interpretation

Given the simplifications and assumptions we have made, our model is hardly unique, but we believe that it includes as much detail as can be supported by our observations. Within the framework of our assumptions, two main conclusions can be drawn:

1. The V04573003 cloud has 0.1 ± 0.02 μm aerosols, in good agreement with Clancy and Sandor (1998). Its optical depth is much larger than that of the $\tau \leqslant 0.05$ mesospheric hazes which have been observed by limb sounders and occultation measurements (Chassefière et al., 1992; Montmessin et al., 2006a,b; Clancy et al., 2007; Fedorova et al., 2009), and twice as large as that proposed by Clancy and Sandor (1998) for their Pathfinder clouds. The complex cloud morphology tends to imply that a condensate is involved. Furthermore, since the mass of condensate is at least four time greater than the maximum amount of water vapor that can be contained in a mesospheric column (this comparison was suggested by P. Gierasch (2006), personal communication), most of the condensate is likely to be CO_2. We have no constraints on the presence or size of any condensation nuclei, other than that they must be smaller than the 0.1 μm overall size of the particles.
2. The V11100003 cloud has large ~1.5 μm particles and a very substantial optical depth of ~0.5 – similar to the particle sizes and optical depths of the OMEGA mesospheric clouds (Montmessin et al., 2007; Määttänen et al., 2010). The V1110003 particle sizes and optical depths also happen to be comparable to those of lower atmosphere water ice clouds. Our radiative transfer models weakly prefer CO_2 over water ice as the composition of these clouds. Even if our models did admit water condensate, the mass of water required would be much higher than the carrying capacity of the mesosphere, and so we have a strong argument for most of the condensate being CO_2, similar once again to the OMEGA mesospheric clouds (Montmessin et al., 2007; Määttänen et al., 2010). Any condensation nuclei present in these clouds is most likely 40% or less of the particle radii and 0.5 μm r_{eff} or less in absolute size, otherwise it would have been detected by one of the infrared instruments.

The substantial difference in measured particle size is consistent with the diversity observed by Chassefière et al. (1992). Despite the large difference in particle size, both the V04573003 and V11100003 clouds, perhaps coincidently, contain condensate equal to 0.07% of the mass of the atmosphere in the 10 km layer below the altitude of the observed features. This means that, because it is 2 scale heights below V04573003, the V11100003 cloud has about 10 times as much mass per unit area. The V04573003 cloud has a 0.1 μm upper limit on the size of the condensation nuclei, which means that, according to Colaprete and Toon (2003) (their Fig. 3), mesospheric temperatures must have transiently reached as low as 90 K near 80 km altitude in order to initiate condensation. This is 5 K below the coldest temperatures observed by Pathfinder, and substantially colder than any other reported mesospheric temperature measurements (*e.g.*, Clancy and Sandor, 1998; Montmessin et al., 2006a; Forget et al., 2009). The V11100003 cloud has a 0.5 μm upper limit on the size of the condensation nuclei, although this upper limit is less secure because it relies on sensitivity of THEMIS-IR, for which we have used only an approximation based on Smith (2004). 0.5 μm condensation nuclei would imply 100 K temperatures at 60 km according to Colaprete and Toon (2003), which is well below any reported temperatures (including those of Pathfinder) at that altitude.

5. Conclusions

THEMIS-VIS was not designed for stereo capability, nor intended to study mesospheric clouds, but nevertheless it can be used to measure mesospheric cloud altitude and zonal velocity. Additionally, the THEMIS-VIS multi-spectral capability and radiance calibration allows it to place constraints on the aerosol properties of the observed cloud. The altitude and velocity measurements have precisions as good as ±1 km and ±10 m/s, respectively (the precision varies from measurement to measurement and is detailed in Tables 5–8). Systematic errors in the THEMIS-VIS camera model add an additional ±1 km and ±10 m/s to the uncertainties, and every 10 m/s of meridional velocity component will produce an error of about 1 km in altitude and 2 m/s in the zonal velocity component.

Using this capability, we have presented exceptionally high resolution horizontally resolved images of verifiably mesospheric clouds, and find that they fall into two distinct classes in the THEMIS-VIS data set: equatorial mesospheric clouds, and northern mid-latitude winter mesospheric clouds.

The THEMIS-VIS equatorial mesospheric clouds are broadly consistent with the Clancy et al. (2007) equatorial mesospheric condensate survey and with the OMEGA and HRSC observations (Montmessin et al., 2007; Määttänen et al., 2010; Scholten et al., 2010) in the sense that they occur in the same regions and seasons

and are likely to be composed of CO_2. They have more in common with the OMEGA and HRSC observations in the sense that fine structure is observed, that the optical depths are high, and that the altitude range (see Scholten et al., 2010) is comparable. The main difference between the THEMIS-VIS equatorial mesospheric cloud observations and those of OMEGA/HRSC is the measurement of particle sizes as small as 0.1 μm in V04573003. The V04573003 case is perhaps most similar to Pathfinder-IMP blue wave clouds (Clancy and Sandor, 1998) in terms of altitude, particle size, optical depth, and proposed composition, although the IMP clouds were found in early morning rather than late afternoon. SPICAM stellar occultation mesospheric condensate clouds (Montmessin et al., 2006a) had particle sizes similar to the V04573003 case, but the altitudes (>90 km), local times (midnight to 1 am), and the opacities (<0.05) were quite different.

We are aware of no previous predictions or observations of discrete mesospheric cloud features in winter mid-latitudes, except for two recently reported OMEGA detections (Määttänen et al., 2010) whose altitudes have not been directly measured. The existence of such clouds places an important new constraint on the cloud formation mechanism or mechanisms in the vicinity of the polar hood, in that they must be operating at altitudes up to 70 km. The observed horizontal, vertical, and temporal distribution of the clouds is most likely controlled by the peculiar pattern of the observations that led to their serendipitous discovery, and thus we have almost no information about the real distribution of this type of cloud, other than that they appear to be visible only in twilight, and, with a detection rate of 17% in Acidalia, fairly common. We do, however, see some evidence that identifies the lineated mesospheric clouds that have 40–55 km altitudes with the polar streak clouds that are ubiquitous in the polar hood.

It is unclear whether the mid-latitude mesospheric clouds and the equatorial mesospheric clouds have anything in common besides the manner in which they were detected. For the equatorial clouds, the Clancy and Sandor (1998) proposal of gravity wave induced supersaturation leading to CO_2 cloud formation is quite consistent with our observations. It is consistent because: (1) our observations suggest CO_2 because the mass of aerosol is too large to be water; (2) both the filamentary and non-filamentary equatorial clouds show some evidence of wave-like patterns (Fig. 7); and (3) the upper limits on the size of any condensation nuclei that might be present, in light of the Colaprete and Toon (2003) calculations of critical supersaturation ratio versus nuclei size, are compatible with CO_2 condensation at gravity wave amplitudes only modestly greater than those observed during the Pathfinder descent.

We have little information on the composition of the mid-latitude mesospheric clouds. The cloud morphologies that we show here may or may not provide insight into their mechanism of formation, and we must of course consider that the clouds at 70 km in altitude may be different in nature than those at 45 km. Given that the mid-latitude winter mesospheric temperatures are observed and modeled to be warmer than those of the aphelion season tropical mesosphere (Smith et al., 2001; Joshi et al., 1995; Forget et al., 2009), CO_2 condensation there is even more problematic, and so these clouds are less likely to be CO_2. Since our modeling of THEMIS-VIS images yielded meaningful constraints on the nature of the equatorial clouds, it seems likely that a radiative transfer model suitable for twilight will ultimately yield similar constraints on the mid-latitude clouds.

Note that one of the two OMEGA winter mid-latitude mesospheric clouds was observed in northern winter (rather than in southern winter mid-latitudes), and at comparable latitude and L_s to our THEMIS-VIS detections (Määttänen et al., 2010). The OMEGA detection positively identifies the cloud as CO_2, which could be evidence in favor of the THEMIS-VIS detections being CO_2 as well. However, lacking a simultaneous HRSC measurement the OMEGA detection only places a lower limit on the cloud's altitude, and so given the relatively warm temperatures at the THEMIS-VIS altitudes, it seems just as likely that the OMEGA cloud is a higher altitude and different phenomenon from the THEMIS-VIS detections.

Explaining the poor match between our equatorial mesospheric velocities and our GCM results is an important challenge for future modeling work. The better match, reported by Määttänen et al. (2010), between HRSC-measured equatorial mesospheric clouds speeds and wind speeds in the González-Galindo et al. (2009) GCM model suggests that extending the model domain to the thermosphere is an important part of the solution. The ideal model would provide a description of gravity wave drag and thermal tides (including tidal momentum transport) that produces *both* the correct wind speeds *and* a combination of temperatures and gravity wave amplitudes sufficient to produce the necessary supersaturation at the altitudes that we observe clouds. We might also hope that such a model would explain the apparent longitudinal asymmetry in the cloud observations. A still more ambitious theoretical or modeling question is the relationship between gravity wave breaking and mesospheric cloud morphology. What would wave-breaking turbulence in mesospheric clouds look like, and is it consistent with our observed morphologies?

As long as THEMIS-VIS continues routine imaging of martian surface features using the green and blue filters, it is likely to continue to discover equatorial mesospheric clouds. The relative allocation of THEMIS-VIS imaging between multi-spectral and monochromatic sequences will obviously greatly affect the rate of detection. Future THEMIS-VIS observations of mid-latitude mesospheric clouds depends on the details of the ODY orbit during the next northern fall-winter period.

The THEMIS-VIS altitude–velocity measurement capability is not in principle limited to mesospheric clouds. At lower altitudes, however, identification of cloud features becomes more problematic, and the confounding effect of nearby surface features on our cross-correlation method becomes more significant. Thus, future work in this direction will involve the development of more sophisticated techniques for feature localization.

Acknowledgments

This research was supported by a grant to Professor Bell from the NASA Mars Odyssey Orbiter Participating Scientist program (JPL Contract 1241434). We also received advice and assistance from numerous individuals, including Peter Gierasch, Don Banfield, Melissa Straussberg, Chase Million, Kerry Cook, James Houck, and from members of the ASU-based THEMIS instrument team: Greg Mehall, Kim Murray, Laural Cherednik, Kelly Bender, and Andras Dombovari.

References

Acton, C.H., 1996. Ancillary data services of NASA's Navigation and Ancillary Information Facility. Planet. Space Sci. 44, 65–70.
Atreya, S.K., Blamont, J.E., 1990. Stability of the martian atmosphere – Possible role of heterogeneous chemistry. Geophys. Res. Lett. 17, 287–290.
Bandfield, J.L., Hamilton, V.E., Christensen, P.R., McSween, H.Y., 2004. Identification of quartzofeldspathic materials on Mars. J. Geophys. Res. 109 (E18), 10009.
Benson, J.L., Bonev, B.P., James, P.B., Shan, K.J., Cantor, B.A., Caplinger, M.A., 2003. The seasonal behavior of water ice clouds in the Tharsis and Valles Marineris regions of Mars: Mars Orbiter Camera Observations. Icarus 165, 34–52.
Bohren, C.F., Huffman, D.R., 1983. Absorption and scattering of light by small particles. Technical report, University of Arizona.
Chassefière, E., Blamont, J.E., Krasnopolsky, V.A., Korablev, O.I., Atreya, S.K., West, R.A., 1992. Vertical structure and size distributions of martian aerosols from solar occultation measurements. Icarus 97, 46–69.
Christensen, P.R., et al., 2003. Morphology and composition of the surface of Mars: Mars Odyssey THEMIS results. Science 300, 2056–2061.
Christensen, P.R., et al., 2004. The Thermal Emission Imaging System (THEMIS) for the Mars 2001 Odyssey mission. Space Sci. Rev. 110, 85–130.
Christensen, P.R. et al., 2005. Evidence for magmatic evolution and diversity on Mars from infrared observations. Nature 436, 504–509.

Clancy, R.T., Sandor, B.J., 1998. CO_2 ice clouds in the upper atmosphere of Mars. Geophys. Res. Lett. 25, 489.
Clancy, R.T., Wolff, M.J., Christensen, P.R., 2003. Mars aerosol studies with the MGS TES emission phase function observations: Optical depths, particle sizes, and ice cloud types versus latitude and solar longitude. J. Geophys. Res. 108 (E9), 5098.
Clancy, R.T., Wolff, M.J., Whitney, B.A., Cantor, B.A., Smith, M.D., 2007. Mars equatorial mesospheric clouds: Global occurrence and physical properties from Mars Global Surveyor Thermal Emission Spectrometer and Mars Orbiter Camera Limb Observations. J. Geophys. Res. 112, E04004.
Colaprete, A., Toon, O.B., 2003. Carbon dioxide clouds in an early dense martian atmosphere. J. Geophys. Res. 108 (E4), 5025.
Conrath, B.J., Pearl, J.C., Smith, M.D., Maguire, W.C., Christensen, P.R., Dason, S., Kaelberer, M.S., 2000. Mars Global Surveyor Thermal Emission Spectrometer (TES) observations: Atmospheric temperatures during aerobraking and science phasing. J. Geophys. Res. 105, 9509–9520.
Efron, B., Tibshirani, R., 1993. An Introduction to the Bootstrap. Chapman and Hall, New York.
Fedorova, A.A., Korablev, O.I., Bertaux, J.-L., Rodin, A.V., Montmessin, F., Belyaev, D.A., Reberac, A., 2009. Solar infrared occultation observations by SPICAM experiment on Mars-Express: Simultaneous measurements of the vertical distributions of H_2O, CO_2 and aerosol. Icarus 200, 96–117.
Forget, F., Hourdin, F., Fournier, R., Hourdin, C., Talagrand, O., Collins, M., Lewis, S.R., Read, P.L., Huot, J.-P., 1999. Improved general circulation models of the martian atmosphere from the surface to above 80 km. J. Geophys. Res. 104, 24155.
Forget, F., Montmessin, F., Bertaux, J.-L., González-Galindo, F., Lebonnois, S., Quémerais, E., Reberac, A., Dimarellis, E., López-Valverde, M.A., 2009. Density and temperatures of the upper martian atmosphere measured by stellar occultations with Mars Express SPICAM. J. Geophys. Res. 114 (E1), E01004.
Gaddis, L., et al., 1997. An overview of the Integrated Software for Imaging Spectrometers (ISIS). Lunar Planet. Sci., 387 (abstract).
Glandorf, D.L., Colaprete, A., Tolbert, M.A., Toon, O.B., 2002. CO_2 snow on Mars and early Earth: Experimental constraints. Icarus 160, 66–72.
González-Galindo, F., Forget, F., López-Valverde, M.A., Coll, M.A.I., 2009. A ground-to-exosphere martian general circulation model: 2. Atmosphere during solstice conditions – thermospheric polar warming. J. Geophys. Res. 114 (E8), 1–21.
Hansen, G.B., 1997. Spectral absorption of solid CO_2 from the ultraviolet to the far-infrared. Adv. Space Res. 20, 1613–1616.
Henyey, L.G., Greenstein, J.L., 1941. Diffuse radiation in the Galaxy. Astrophys. J. 93, 70–83.
Holton, J.R., 1983. The influence of gravity wave breaking on the general circulation of the middle atmosphere. J. Atmos. Sci. 40, 2497–2507.
Hunten, D.M., Turco, R.P., Toon, O.B., 1980. Smoke and dust particles of meteoric origin in the mesosphere and stratosphere. J. Atmos. Sci. 37, 1342–1357.
Inada, A., Richardson, M.I., McConnochie, T.H., Strausberg, M.J., Wang, H., Bell, J.F., 2007. High-resolution atmospheric observations by the Mars Odyssey Thermal Emission Imaging System. Icarus 192, 378–395.
Jaquin, F., 1988. Very high elevation water ice clouds on Mars: Their morphology and temporal behavior. In: Lunar and Planetary Institute, MECA Workshop on Atmospheric H_2O Observations of Earth and Mars. Physical Processes, Measurements and Interpretations, pp. 58–61.
Jaquin, R.F.I., 1989. The middle martian atmosphere. Ph.D. thesis, Cornell University.
Jaquin, F., Gierasch, P., Kahn, R., 1986. The vertical structure of limb hazes in the martian atmosphere. Icarus 68, 442–461.
Joshi, M.M., Lawrence, B.N., Lewis, S.R., 1995. Gravity wave drag in three-dimensional atmospheric models of Mars. J. Geophys. Res. 100, 21235–21246.
Klostermeyer, J., 2002. Noctilucent clouds getting brighter. J. Geophys. Res. 107 (D14), 4195.
Kokhanovsky, A.A., 2005. Microphysical and optical properties of noctilucent clouds. Earth Sci. Rev. 71, 127–146.
Lee, C. et al., 2009. Thermal tides in the martian middle atmosphere as seen by the Mars Climate Sounder. J. Geophys. Res. 114 (E13), E03005.
Lellouch, E., Rosenqvist, J., Goldstein, J.J., Bougher, S.W., Paubert, G., 1991. First absolute wind measurements in the middle atmosphere of Mars. Astrophys. J. 383, 401–406.
Lewis, S.R., Collins, M., Read, P.L., Forget, F., Hourdin, F., Fournier, R., Hourdin, C., Talagrand, O., Huot, J.-P., 1999. A climate database for Mars. J. Geophys. Res. 104, 24177.
Määttänen, A., Vehkamäki, H., Lauri, A., Merikallio, S., Kauhanen, J., Savijärvi, H., Kulmala, M., 2005. Nucleation studies in the martian atmosphere. J. Geophys. Res. 110, 02002.
Määttänen, A. et al., 2010. Mapping the properties of the mesospheric CO_2 clouds observed by Mars Express: OMEGA and HRSC observations and a comparison to the LMD-MGCM. Icarus 209 (2), 452–469.
McConnochie, T.H., Bell III, J.F., Savransky, D., Mehall, G., Caplinger, M., Christensen, P.R., Cherednik, L., Bender, K., Dombovari, A., 2006. Calibration and in-flight performance of the Mars Odyssey Thermal Emission Imaging System visible imaging subsystem (THEMIS VIS). J. Geophys. Res. 111 (E10), 6018.
Montmessin, F., Bertaux, J., Quemerais, E., Korablev, O., Rannou, P., Forget, F., Perrier, S., Fussen, D., Lebonnois, S., Reberac, A., 2006a. Subvisible CO_2 ice clouds detected in the mesosphere of Mars. Icarus 183 (2), 403–410.
Montmessin, F., Quémerais, E., Bertaux, J.L., Korablev, O., Rannou, P., Lebonnois, S., 2006b. Stellar occultations at uv wavelengths by the SPICAM instrument: Retrieval and analysis of martian haze profiles. J. Geophys. Res. 111, E09S09.
Montmessin, F., Gondet, B., Bibring, J.-P., Langevin, Y., Drossart, P., Forget, F., Fouchet, T., 2007. Hyperspectral imaging of convective CO_2 ice clouds in the equatorial mesosphere of Mars. J. Geophys. Res. 112, E11S90.
Moreno, R., Lellouch, E., Forget, F., Encrenaz, T., Guilloteau, S., Millour, E., 2009. Wind measurements in Mars' middle atmosphere: IRAM Plateau de Bure interferometric CO observations. Icarus 201, 549–563.
Press, W.H., Teukolsky, S.A., Vetterling, W.T., Flannery, B.P., 1992. Numerical Recipes in C: The Art of Scientific Computing, second ed. Cambridge University Press.
Richardson, M., Toigo, A., Newman, C., 2007. PlanetWRF: A general purpose, local to global numerical model for planetary atmospheric and climate dynamics. J. Geophys. Res. 112, E09001.
Scholten, F., Hoffmann, H., Määttänen, A., Montmessin, F., Gondet, B., Hauber, E., 2010. Concatenation of HRSC colour and OMEGA data for the determination and 3D-parameterization of high-altitude CO_2 clouds in the martian atmosphere. Planet. Space Sci. 58 (10), 1207–1214.
Smith, M.D., 2004. Interannual variability in TES atmospheric observations of Mars during 1999–2003. Icarus 167, 148–165.
Smith, P.H. et al., 1997. Results from the Mars Pathfinder Camera. Science 278, 1758.
Smith, M.D., Pearl, J.C., Conrath, B.J., Christensen, P.R., 2001. Thermal Emission Spectrometer results: Mars atmospheric thermal structure and aerosol distribution. J. Geophys. Res. 106, 23929–23946.
Smith, M.D., Bandfield, J.L., Christensen, P.R., Richardson, M.I., 2003. Thermal Emission Imaging System (THEMIS) infrared observations of atmospheric dust and water ice cloud optical depth. J. Geophys. Res. 108 (E11), 5115.
Sonnabend, G., Wirtz, D., Vetterle, V., Schieder, R., 2005. High-resolution observations of martian non-thermal CO_2 emission near 10 μm with a new tuneable heterodyne receiver. Astron. Astrophys. 435, 1181–1184.
Stamnes, K., Tsay, S.-C., Jayaweera, K., Wiscombe, W., 1988. Numerically stable algorithm for discrete-ordinate-method radiative transfer in multiple scattering and emitting layered media. Appl. Opt. 27, 2502–2509.
Titus, T.N., Kieffer, H.H., Christensen, P.R., 2003. Exposed water ice discovered near the south pole of Mars. Science 299, 1048–1051.
Torson, J.M., Becker, K.J., 1997. ISIS – A software architecture for processing planetary images. Lunar Planet. Sci., 1443 (abstract).
Wang, H., Ingersoll, A.P., 2002. Martian clouds observed by Mars Global Surveyor Mars Orbiter Camera. J. Geophys. Res. 110 (E10), 5078.
Wang, H., Zurek, R.W., Richardson, M.I., 2005. Relationship between frontal dust storms and transient eddy activity in the northern hemisphere of Mars as observed by Mars Global Surveyor. J. Geophys. Res. 110, E07005.
Warren, S.G., 1984. Optical constants of ice from the ultraviolet to the microwave. Appl. Opt. 23, 1206–1225.
Wolff, M.J., James, P.B., Todd Clancy, R., Lee, S.W., 1999. Hubble Space Telescope observations of the martian aphelion cloud belt prior to the Pathfinder mission: Seasonal and interannual variations. J. Geophys. Res. 104, 9027–9042.
Wolff, M.J. et al., 2006. Constraints on dust aerosols from the Mars Exploration Rovers using MGS overflights and mini-TES. J. Geophys. Res. 111, E12S17.
Zurek, R.W., 1992. Comparative Aspects of the Climate of Mars – An Introduction to the Current Atmosphere. In: Mars. The University of Arizona Press, Tucson, AZ, pp. 799–817.